International Journal of Biological Macromolecules 332 (2025) 148563

Contents lists available at ScienceDirect

International Journal of Biological Macromolecules

journal homepage: www.elsevier.com/locate/ijbiomac

Biogenic/chitosan/bamboo fiber ternary bio-nanocomposite: Dual-functional platform for environmental and biomedical applications

Raji Ramachandran [a], P. Saravanakumar [b], M. Mathina [c], E. Shinyjoy [d], Zarlina Zainuddin [e], R.K. Govindarajan [f], Chinnaperumal Kamaraj [g,*], Dhanaraj Gopi [h,*], Ratna Surya Alwi [a,*]

[a] Research Centre for Computing, National Research and Innovation Agency (BRIN), Jl. Raya Jakarta-Bogor KM 46, Cibinong, Indonesia
[b] Department of Chemistry, Government Arts and Science College Malayadipudur, Komarapalayam, Sathyamangalam – Erode, 638 401, Tamil Nadu, India
[c] Department of Chemistry, Purathchi Thalaivar M.G.R Govt. Arts and Science College, Thirupulivanam, Uthiramerur, Kancheepuram, Tamil Nadu, India
[d] Department of Chemistry, Vinayaka Mission's Kirupananda Variyar Arts and Science College, Vinayaka Mission's Research Foundation, Salem, Tamil Nadu, India
[e] Research Centre for Polymer Technology, National Research and Innovation Agency, Indonesia
[f] Department of Biotechnology, Karpagam Academy of Higher Education, Eachanari, Coimbatore, Tamil Nadu, India, 641021
[g] Interdisciplinary Institute of Indian System of Medicine (IIISM), Directorate of Research, SRM Institute of Science and Technology, Kattankulathur, 603203, Tamil Nadu, India
[h] Department of Chemistry, Periyar University, Salem, 636 011, Tamil Nadu, India

ARTICLE INFO

Keywords:
Bamboo fiber
Chitosan
Degradation
Methylene blue
Nanocomposite
Snail shell

ABSTRACT

Quality of life depend on access to water that is free from contaminants and harmful microorganisms. However, industrialization, population growth, and environmental pollution have severely impacted water quality worldwide. This study presents a novel, biodegradable, and cost-effective ternary bio-nanocomposite composed of macromolecules of cerium-substituted hydroxyapatite (Ce-HAP), chitosan (CS), and bamboo fiber (BF). The Ce-HAP/CS/BF bio-nanocomposite was derived from renewable biogenic sources such as snail shells, CS, and BF. It was designed for applications in both environmental remediation and biomedical fields. The physicochemical characterization of Ce-HAP/CS/BF was performed using FTIR, XRD, HRSEM, TEM, EDX, TGA/DTA, UV-DRS, and XPS, confirming the successful integration of all components along with enhanced crystallinity, porosity, and thermal stability. Photocatalytic studies revealed effective degradation of methylene blue (MB) dye, with hydroxyl radicals (•OH) identified as the primary active species. Antibacterial assays demonstrated strong inhibitory effects against *Escherichia coli* and *Staphylococcus aureus*. Cytocompatibility evaluation using MG63 osteoblast-like cells showed over 90 % cell viability at all tested concentrations, confirming excellent biocompatibility. Furthermore, swelling and degradation studies in simulated body fluid indicated suitable water absorption and controlled degradation rates. Overall, the Ce-HAP/CS/BF bio-nanocomposite exhibits great potential as a sustainable material for wastewater treatment and bone tissue engineering, offering a multifunctional approach to address both environmental and healthcare challenges.

1. Introduction

In recent years, the production of textiles and clothing, medicinal supplies, cosmetics, and pigments has been the primary purpose for the use of dyes and colouring agents [1]. About 15 % of the unprocessed dyes used during the dyeing process are directly released into the

Abbreviations: HAP, hydroxyapatite; Ca^{2+}, calcium ions; PO_4^{3-}, phosphate ions; OH^-, hydroxide ions; CO_3^{2-}, carbonate ions; Ce, cerium; BF, bamboo fiber; CS, chitosan; MB, methylene blue; SBF, simulated body fluid; FT-IR, Fourier-transform infrared spectroscopy; FESEM, field emission scanning electron microscopy; EDS, energy-dispersive X-ray spectroscopy; UV-DRS, ultraviolet-visible diffuse reflectance spectroscopy; XPS, X-ray photoelectron spectroscopy; TGA, thermogravimetric analysis; DTA, differential thermal analysis; HOS, human osteosarcoma cell lines (MG63); EMEM, Eagle's minimum essential medium; FBS, fetal bovine serum; MTT, 3-(4,5-dimethylthiazol-2-yl)-2,5-diphenyltetrazolium bromide; $(NH_4)_2HPO_4$, diammonium hydrogen phosphate; NaOH, sodium hydroxide; HCl, hydrochloric acid; H_2SO_4, sulfuric acid; HNO_3, nitric acid; $AgNO_3$, silver nitrate and; DI, deionized water; $CaCO_3$, calcium carbonate; CaO, calcium oxide; EDTA, ethylenediaminetetraacetic acid; IPA, isopropyl alcohol; BQ, benzoquinone; AO, ammonium oxalate; •OH, hydroxyl radicals; PBS, phosphate-buffered saline; BMSCs, bone marrow stem cells; UV, ultraviolet light.

* Corresponding authors.
E-mail addresses: kamarajc@srmist.edu.in (C. Kamaraj), gopi@periyaruniversity.ac.in (D. Gopi), ratn017@brin.go.id (R.S. Alwi).

https://doi.org/10.1016/j.ijbiomac.2025.148563
Received 16 May 2025; Received in revised form 14 August 2025; Accepted 26 October 2025
Available online 27 October 2025

environment, posing a serious threat to ecosystems [2]. These pigments are usually highly stable and do not readily degrade under natural conditions [3]. Therefore, in the past few decades, it has become increasingly important to develop effective processes for removing dyes from aquatic environments. Such pollutants can accumulate in the cell membranes of living organisms and enter the food chain, constituting a significant global threat to biodiversity [4]. Organic-coloured chemical dyes enter water bodies through effluents from various industries, including paper, textiles, bleaching, pharmaceuticals, leather, cosmetics, tanning, plastics, and rubber manufacturing [5–10]. These industries consistently use large quantities of synthetic dyes, producing substantial amounts of coloured effluents that are harmful to both human health and aquatic ecosystems [11–14]. Methylene blue (MB), a heterocyclic aromatic compound, is one of the most widely used synthetic dyes in various fields, including biology and chemistry [15]. In its solid form, MB is a dense, odourless, deep-green substance which produces a blue-coloured solution when dissolved in water. It is extensively used for dyeing wool and cotton fabrics, paper products, and as a temporary hair dye [16–20]. However, MB can have harmful side effects excessive exposure may impair vision, and frequent ingestion can lead to mental health issues, nausea, and vomiting.

Maintaining ecosystem health and preserving biological cycles requires preventing the excessive release of hazardous materials into aquatic environments [21]. Wastewater containing dyes can be treated using various techniques, such as coagulation, membrane filtration, electrolysis, biological treatment, photocatalytic oxidation, and adsorption [22–27]. Among these, photocatalytic degradation is frequently employed due to its advantages, including low cost, operational simplicity, and environmental friendliness [28]. Activated charcoal is often used for dye removal; however, it can be expensive. As a result, numerous low-cost and readily available adsorbent materials such as rice husks, coffee husks, pine cones, sugarcane bagasse, clays, walnut shells, and calcium phosphates have been investigated for this purpose [29–31].

Effective photocatalysts are capable of permanently breaking down organic pollutants in aqueous solutions in a cost-effective, environmentally friendly manner, and under visible-light activation. Metal oxide semiconductors hold great potential as photocatalysts due to their excellent optoelectronic stability and favourable physical and chemical properties. However, conventional materials such as ZnO and TiO_2 are primarily active only in the UV spectrum because of their wide bandgap and rapid electron–hole recombination. The present study focuses on the development of environmentally friendly hydroxyapatite-based catalysts to overcome these limitations [32].

Hydroxyapatite ($Ca_{10}(PO_4)_6(OH)_2$, HAP) is a principal component of bones and teeth, valued for its environmental benignity, biological activity, and excellent biocompatibility, making it highly suitable for musculoskeletal therapies. Beyond biomedical applications, HAP possesses unique properties, including a large specific surface area, low solubility in water, structural stability, and high thermal conductivity that enable its use as a green photocatalyst for degrading harmful pigment molecules. For instance, combining HAP with TiO_2 nanoparticles under simulated solar light irradiation has been shown to effectively remove nitric oxide from the environment. Its photocatalytic performance is further enhanced by phosphate sites in HAP, which promote the generation of superoxide radicals, thereby accelerating pollutant degradation. Moreover, HAP a high adsorptive capacity offers a dual advantage: it can capture and concentrate pollutants on its surface, enhancing both the efficiency and selectivity of photocatalytic reactions. This synergy of adsorption and photocatalysis makes HAP an attractive and sustainable material for environmental remediation applications.

During the photocatalytic process, oxygen vacancies on the outermost layer of HAP act as electron acceptors [33–35]. However, due to its wide bandgap, HAP alone is often incapable of effectively degrading organic pigments under ultraviolet (UV) irradiation [36]. To enhance its efficiency under UV light and reduce degradation time, researchers have sought to combine HAP with optically active materials. For example, carbon-doped HAP exhibits improved photocatalytic performance for the decomposition of methylene blue (MB) dye under UV irradiation. Furthermore, to enhance the functionality of HAP, various semiconductor-based materials such as Ti, Ag, Fe, and Co are currently being investigated as dopants or composite partners.

Unfortunately, due to the cost of the chemical precursors used as sources of phosphate and calcium, synthetically produced HAP is often expensive. Consequently, biogenic waste materials such as mussel shells, oyster shells, fish scales, biomass ash, and snail shells are gaining significant scientific attention as low-cost, renewable sources for producing value-added HAP. Among these, snail shell-derived HAP has recently attracted particular interest. Several studies have reported that HAP is one of the most versatile biomaterials, with applications spanning wastewater treatment, electronics, and biomedical therapies [37].

For various photocatalytic applications, HAP has been combined with other functional materials. For instance, the incorporation of semiconductor nanoparticles onto the HAP surface produces composite photocatalysts with strong photodegradation performance under UV irradiation [38]. Consequently, HAP/semiconductor composites have emerged as reliable catalysts for the photocatalytic decomposition of pollutants, receiving growing research attention [39].

Bamboo is a plentiful, inexpensive, and environmentally friendly biomass resource rich in lignocellulose. It has a wide range of uses, including as a food source, construction material, and versatile natural biomass. However, bamboo processing generates large quantities of waste. A significant proportion of lignocellulose is found in bamboo fiber [40], which can be converted into high-value lignocellulose derivatives. Due to its small particle size, irregular shape, and porous structure, raw bamboo fiber can be challenging to utilize directly for specific applications. Therefore, further research on bamboo waste is essential to identify alternative value-added uses [41].

In wastewater treatment, lignocellulose-based adsorbents such as cellulose, activated carbon, and lignin-derived materials are well established [41,42]. Adsorbents derived from bamboo possess excellent socioeconomic and environmental benefits. However, their small particle size makes them difficult to separate from treated effluents [43]. An effective strategy to overcome this limitation is to incorporate bamboo fiber (BF) into a polymer matrix. Such a matrix not only facilitates the easy separation of adsorbents from water but also enhances their interaction with charged contaminants. Furthermore, desirable features of the polymer matrix include high porosity and strong durability in aqueous environments [44–47].

Fortunately, structural modification of HAP has been shown to significantly improve its photosensitivity. However, its inherently low surface adsorption capacity and the rapid recombination of electron–hole pairs can limit its photocatalytic efficiency. To overcome these limitations, incorporating polymeric materials can enhance its properties and overall photocatalytic performance [48]. In this regard, several studies have reported that metal oxide/polymer composites exhibit improved sorption capacity.

Biopolymers are highly versatile and can readily form chemical interactions with contaminants [49]. Among them, chitosan (CS) is a particularly promising polymer that has been shown to enhance pollutant degradation when incorporated into photocatalytic materials [50]. Due to its amino functional groups, CS acts as a natural bioadsorbent and is frequently employed as a substrate in photocatalytic studies [51,52].

Recent advances in nanostructured photocatalysts have demonstrated promising potential for both environmental and biomedical applications. For example, a hybrid MWCNTs/g-C_3N_4/chitosan nanocomposite thin film (NCTF), synthesized via solution casting, exhibited excellent visible-light-driven phenol degradation and retained over 80 % efficiency after five cycles [53]. Similarly, a *Z*-scheme g-C_3N_5@Bi_2WO_6/PPy photocatalyst displayed superior charge transfer and

visible-light activity, achieving over 96 % and 98 % degradation of Rhodamine B and Methylene Blue, respectively, within 60 min, with strong stability and involvement of $O_2\bullet^-$ and h^+ species [54].

Green-synthesized CdS quantum dots prepared using *Crocus sativus* L. extract showed 92 % Rhodamine B degradation under UV light, significant antibacterial activity, and 79 % cytotoxicity against MCF-7 cells, underscoring their potential for both photocatalytic and biomedical applications [55]. Furthermore, a ternary CTS–SnO_2–MWCNTs nanohybrid, developed via an interfacial engineering approach, demonstrated enhanced methylene blue degradation (97.59 %) and adsorption (84.24 %), along with excellent antibacterial activity and stability, providing a noble-metal-free alternative for efficient photocatalysis [56].

This research incorporated bamboo fiber (*Bambusa vulgaris*) into a Ce-HAP/chitosan/bamboo fiber (Ce-HAP/CS/BF) ternary bionanocomposite to develop a multifunctional material for both environmental and biomedical applications. The primary objective was to fabricate a cost-effective, biogenic composite exhibiting strong antimicrobial activity against clinical pathogens, high biocompatibility for bone and tissue engineering, and efficient photocatalytic performance for the removal of methylene blue (MB) dye from wastewater. The study emphasized sustainability by utilizing natural and waste-derived materials to create low-cost adsorbents with high pollutant removal efficiency. Furthermore, the photocatalytic degradation mechanism of cationic pollutants was investigated, highlighting the generation and role of reactive species particularly hydroxyl radicals in the dye decomposition process.

2. Materials and methods

2.1. Chemicals

Cerium (III) nitrate pentahydrate ($Ce(NO_3)_3{\cdot}5H_2O$), hydrochloric acid (HCl), sulfuric acid (H_2SO_4), concentrated nitric acid (HNO_3), Methyl Blue (MB), The different scavengers such as disodium ethylenediaminetetraacetate (EDTA-2Na), 1,4-benzoquinone (BQ) and isopropyl alcohol (IPA) silver nitrate ($AgNO_3$), Diammonium hydrogen orthophosphate $(NH_4)_2HPO_4$, sodium hydroxide (NaOH), $5H_2O$, Chitosan (80–95 % deacetylated), and acetic acid were purchased from Sigma Aldrich. Generally available dead snail shells were collected from a local paddy cultivation area in Cibinong, Indonesia. All chemicals were used without further purification. Deionized (DI) water was used in all the experiments.

2.2. Extraction of calcium oxide from snail shell

The snail shells ($CaCO_3$, 95–99 %) were thoroughly washed with running water to remove mud and other impurities, followed by several washes with deionized (DI) water. They were then boiled at 100 °C for 4 h. Next, the shells underwent ultrasonic treatment in an ethanol–water mixture for 2 h to remove any fibrous layers and were subsequently dried in a hot-air oven at 90 °C for 5 h. The dried shells were crushed into small pieces, placed in a silica crucible, and calcined in a muffle furnace at 1000 °C for 3 h to produce calcium oxide (CaO). After heating, the shells turned pure white. The furnace was allowed to cool to ambient temperature, and the obtained white powder was mechanically ground with an agate pestle and mortar to obtain fine CaO powder. This CaO was then converted into calcium nitrate for use in the subsequent biocomposite preparation.

2.3. Snail shell-derived cerium-substituted HAP (Ce-HAP)

To prepare Ce-HAP, CaO (0.3 M) and $Ce(NO_3)_3{\cdot}6H_2O$ (0.05 M) were first mixed thoroughly. Subsequently, $(NH_4)_2HPO_4$ was added dropwise to the above mixture at ambient temperature until the stoichiometric proportion of $(Ca + Ce)/P = 1.67$ for Ce-HAP was achieved. The pH of the resulting solution was adjusted to 4.5 using 0.1 M NaOH. The reaction mixture was continuously stirred using a magnetic stirrer for 24 h. The final product was then filtered and washed several times with deionized water, ethanol, and water to obtain pure Ce-HAP. The resulting white precipitate was collected and used for further processing.

2.4. Preparation of Ce-HAP/CS solution

A chitosan (CS) solution was prepared by dissolving 0.5 g of CS powder in 20 mL of 2 % (*v*/v) aqueous acetic acid under constant stirring for 2 h. Cerium-substituted Hydroxyapatite (Ce-HAP) powder was then gradually added to the CS solution, and the mixture was stirred for an additional 1 h at room temperature to obtain a uniform and homogeneous suspension.

2.5. Preparation of BF extract

Bamboo fibres (BF) were collected from the BRIN Campus, Cibinong, Indonesia. The fibres were cut into lengths of approximately 0.5–0.8 mm, rinsed with deionized water for 10 min, and dried in an oven at 80 °C for 24 h to remove moisture. Ten grams of the dried BF were crushed and boiled in a 10 % (*w/v*) sodium hydroxide solution for 1 h. The BF were then repeatedly washed with deionized water until the wash water reached pH 7, followed by drying again at 80 °C for 24 h. The treated fibres were collected by filtration using Whatman filter paper and cooled to room temperature. Finally, the fibres were subjected to centrifugation at 10,000 rpm, and the supernatant was collected for further processing.

2.6. Synthesis of Ce-HAP/CS/BF ternary nanocomposite

The Ce-HAP extract prepared in Section 2.3 was added dropwise to the Ce-HAP/CS solution (Section 2.4) and simultaneously added dropwise to the BF suspension under continuous magnetic stirring. This addition resulted in the formation of a dirty-white precipitate. The mixture was then ultrasonicated for 2 h to promote uniform dispersion, followed by magnetic stirring for 24 h to ensure complete interaction among the components. An additional ultrasonication step for 1 h was carried out to achieve a homogeneous mixture. The resulting product was filtered, dried at 400 °C, and ground into a fine powder to obtain the Ce-HAP/CS/BF ternary nanocomposite. A schematic representation of the synthesis process is shown in Fig. 1.

2.7. Characterization techniques

2.7.1. Physio-chemical characterizations

The synthesized HAP, Ce-HAP, Ce-HAP/CS, and Ce-HAP/CS/BF nanocomposites were subjected to comprehensive physicochemical characterization to determine their functional groups, crystal structures, surface morphologies, elemental compositions, and optical properties. Fourier-transform infrared (FT-IR) spectroscopy was performed using an Impact 400 D Nicolet spectrometer via the KBr pellet method over a wavenumber range of 400–4000 cm^{-1}. Crystalline structures were analyzed using X-ray diffraction (XRD) with an X'Pert PANalytical diffractometer operating at room temperature in the 2θ range of 20°–80°, employing Cu Kα radiation. Surface morphology and microstructural features were examined using high-resolution field-emission scanning electron microscopy (HRSEM), while particle morphology was further confirmed via transmission electron microscopy (TEM). Elemental composition and distribution were analyzed using energy-dispersive X-ray spectroscopy (EDX), and the quantitative elemental content was determined using inductively coupled plasma optical emission spectroscopy (ICP-OES). Thermal stability and decomposition behaviour were assessed using thermogravimetric analysis and differential thermal analysis (TGA/DTA). Optical properties and band gap estimations were obtained from ultraviolet-visible diffuse reflectance

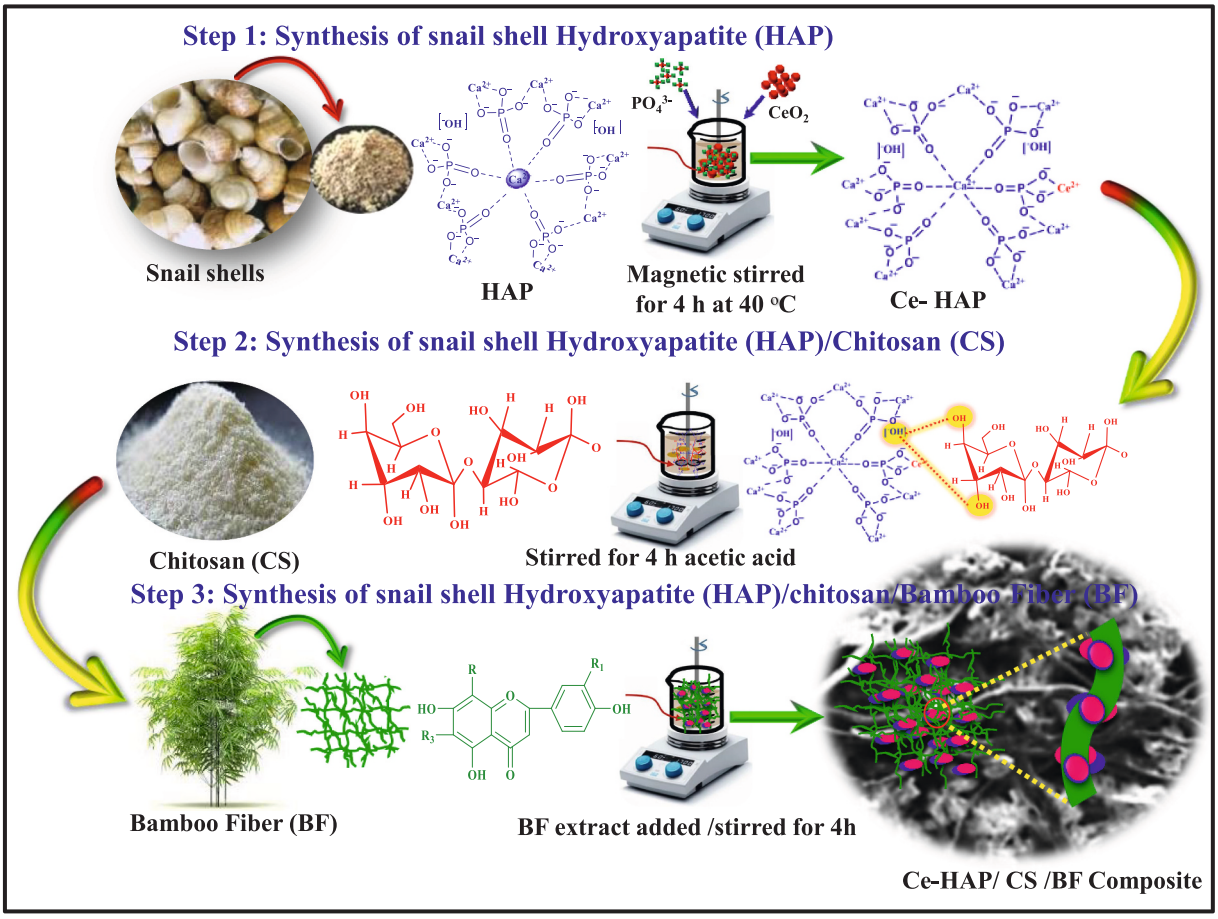

Fig. 1. Schematic representation of the synthesis of Ce-HAP/CS/BF ternary nanocomposite.

spectroscopy (UV-DRS), and surface elemental states along with chemical bonding environments were investigated by X-ray photoelectron spectroscopy (XPS).

2.8. Biological characterizations

2.8.1. Antibacterial activity

Employing the established diffusion method and standard protocols, the antimicrobial activity of the as-synthesized HAP, Ce-HAP, Ce-HAP/CS, and Ce-HAP/CS/BF nanocomposites was evaluated against two bacterial strains: Gram-positive *Staphylococcus aureus* (ATCC 25923) and Gram-negative *Escherichia coli* (ATCC 25922). Whatman filter paper discs, each with a diameter of 6 mm, were prepared and impregnated with two different concentrations (50 and 100 mg/μL) of the respective nanocomposites. The discs were placed on the inoculated Petri plates at equal distances apart, followed by incubation at 37 °C for

24 h. After incubation, the zones of inhibition formed around the discs were measured to assess antibacterial efficacy against both bacterial strains.

2.8.2. Swelling and degradation behaviour

Swelling tests were carried out for HAP, Ce-HAP, Ce-HAP/CS, and Ce-HAP/CS/BF nanocomposite samples. In this assay, 10 mL of simulated body fluid (SBF) was used to submerge each sample, and measurements were taken at 0, 2, 4, 6, 8, 10, 12, and 14 days after immersion. Each sample was weighed prior to immersion, and after the designated incubation period, the specimens were retrieved, excess solution was removed by air-drying at 36 °C, and the samples were reweighed to determine swelling. The degradation behaviour of the nanocomposites was also evaluated under the same conditions, and the results were expressed along with their respective standard deviations.

2.8.3. In vitro cytotoxicity study with HOS MG63 cells

MG63 osteoblast cells, a human osteosarcoma cell line (HOS MG63, ATCC CRL-1427™), were used to evaluate the in vitro cytocompatibility of the Ce-HAP/CS/BF nanocomposite samples. The viability of cells colonizing the samples was assessed using a modified MTT assay (3-[4,5-dimethylthiazol-2-yl]-2,5-diphenyl tetrazolium bromide). For the assay, HOS MG63 cells were seeded in 12-well plates at a density of 1×10^4 cells/mL. After 24 h of incubation, MTT solution was added, and the cells were further incubated for 1, 4, and 7 days. Following the incubation, the absorbance of each well was recorded, and cell viability (%) was calculated relative to control wells using the equation:

$$\%\text{Cell viability} = [\text{A}]\ \text{Test}/[\text{A}]\ \text{Control} \times 100.$$

2.9. Statistical analysis

Experimental data are presented as mean ± SD values and interpreted using GraphPad Prism 8.3 (GraphPad Software, San Diego, CA, United States) and Origin Pro (Origin Lab Corporation, Northampton, MA, USA).

3. Results and discussion

3.1. FT-IR analysis

FTIR spectroscopy was employed to investigate the chemical bonding and structural evolution of the synthesized nanocomposites. The FTIR spectra for HAP, Ce-HAP, Ce-HAP/CS, and Ce-HAP/CS/BF

nanocomposites are presented in Fig. 2(a-d). In the spectrum of pure HAP, Fig. 2(a), characteristic vibrational modes of phosphate (PO_4^{3-}) groups were observed. The prominent peaks at 1023, 961, 603, 563, and 453 cm^{-1} correspond to asymmetric and symmetric stretching and bending vibrations of the PO_4^{3-} tetrahedral units. Additionally, a broad absorption band at 3575 cm^{-1} and a bending mode at 1622 cm^{-1} were attributed to stretching and bending vibrations of adsorbed hydroxyl (OH) groups and water molecules, respectively. Upon cerium substitution in the HAP lattice Fig. 2(b), minor shifts and peak broadening were observed, particularly near 1644 cm^{-1} and 1004 cm^{-1}, suggesting successful incorporation of Ce^{3+}/Ce^{4+} ions and associated lattice distortion. In the FTIR spectrum of the Ce-HAP/CS nanocomposite Fig. 2 (c), additional peaks appeared at 2936 cm^{-1} and 1627 cm^{-1}, attributed to C—H stretching and amide (C=O) stretching vibrations, respectively, indicating the presence of chitosan. The characteristic broad (OH) stretching band around 3456 cm^{-1} further confirms chitosan incorporation. The spectrum of Ce-HAP/CS/BF nanocomposite Fig. 2(d) revealed more complex features. Peaks at 3422 cm^{-1} (OH), and N—H stretching, 2864 and 2409 cm^{-1} (C—H stretching) and a strong band at 1734 cm^{-1}C=O stretching from esters or carboxylates suggest the presence of BF components. Additional peaks at 1635 cm^{-1} (C=C or aromatic skeletal vibrations), 1412 cm^{-1} (CO_3^{2-} bending), 1328 cm^{-1} (C—H bending), 1038 cm^{-1} (C–O–C asymmetric stretching), and 1038 cm^{-1} (C—O stretching) confirm the inclusion of polysaccharide and lignocellulosic structures from BF. Notably, the retention of PO_4^{3-} peaks at 563 and 603 cm^{-1} and their slight shifting indicates sustained HAP structure with interfacial interaction among the Ce-HAP/CS/BF nanocomposite. The presence of new functional groups shifts in vibrational bands, and broadening effects suggest strong hydrogen bonding and electrostatic interactions among the nanocomposite constituents. These spectral features collectively confirm the successful formation of an integrated Ce-HAP/CS/BF nanocomposite system with robust interfacial compatibility between the biopolymeric and inorganic phases.

3.2. X-ray diffraction studies

Fig. 3 (a-d) illustrates the results of the XRD phase evaluation of the as-synthesized HAP, Ce-HAP, Ce-HAP/CS, and Ce-HAP/CS/BF materials. Fig. 3 (a) The XRD pattern of hydroxyapatite (HAP) exhibits well-defined peaks at 2θ = 26.06°, 31.94°, 33.17°, 34.29°, and 39.94°, corresponding to the (211), (300), (112), (306), (221), (222), and (213) crystal planes. These peaks confirm the formation of a pure hexagonal phase HAP structure without any detectable secondary phases in good agreement with JCPDS card No. 09-0432. Fig. 3(b). In the cerium-doped HAP (Ce-HAP), diffraction peaks with slight shifts in 2θ positions and notable broadening, indicating lattice distortion due to cerium incorporation. The corresponding crystallographic planes are indexed as (122), (125), (034), (128), (131), (310), (238), (004), and (322). These peaks' reduced intensity and broadened nature further support the successful substitution of Ce ions into the HAP crystal lattice also consistent with JCPDS card No. 09-0432 for the HAP phase. Fig. 3(c). The XRD pattern of the Ce-HAP/chitosan (CS) composite reveals diffraction peaks at 2θ = 20.24°, 25.84°, 28.78°, 29.28°, 31.63°, 37.7°, and 42.18°, which correspond to the (202), (101), (300), (211), (311), (320), and (402) planes. The additional peaks observed at 47.24°, 48.30°, and 53.16° align well with the ICDD reference card No. 78-1420, confirming the presence of CS in the composite Fig. 3(d) The XRD pattern of the Ce-HAP/CS/BF nanocomposite shows diffraction peaks at

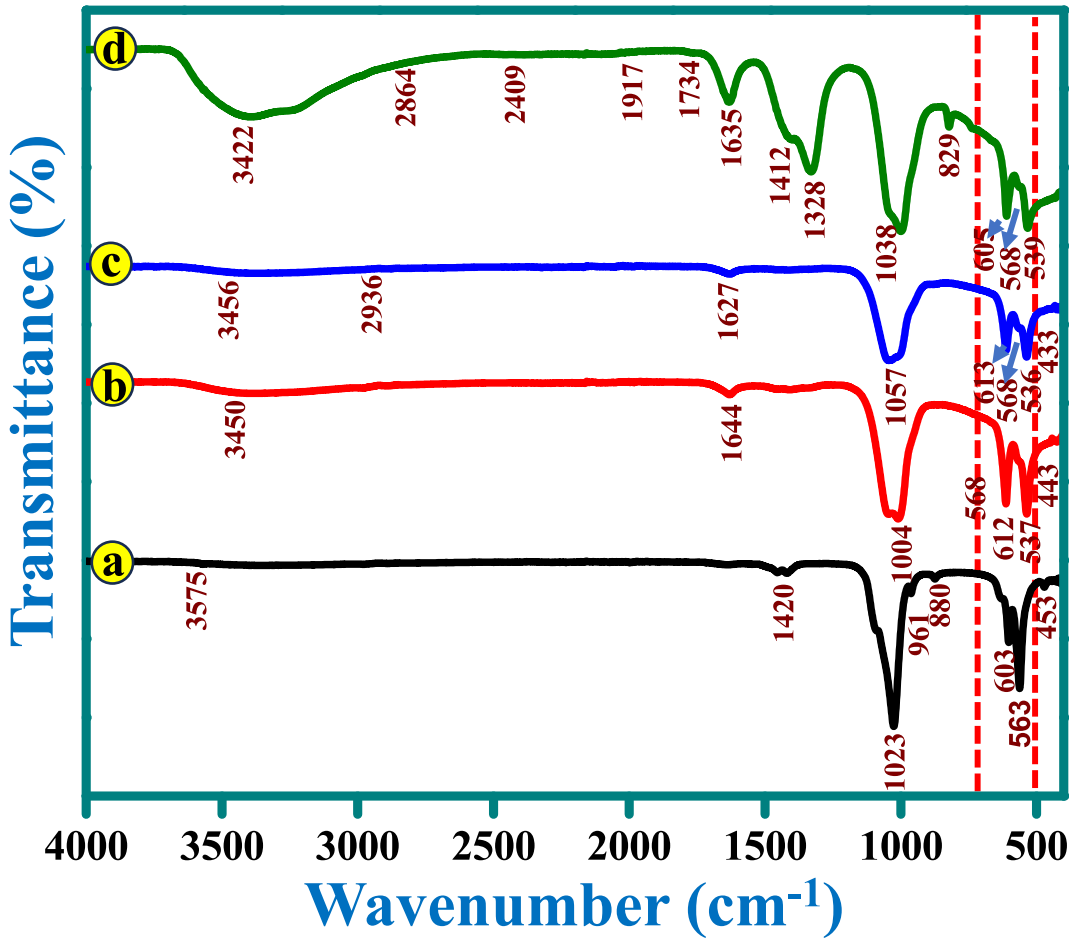

Fig. 2. FT-IR spectra of (**a**) HAP, (**b**) Ce-HAP, (**c**) Ce-HAP/CS, and (**d**) Ce-HAP/CS/BF nanocomposite.

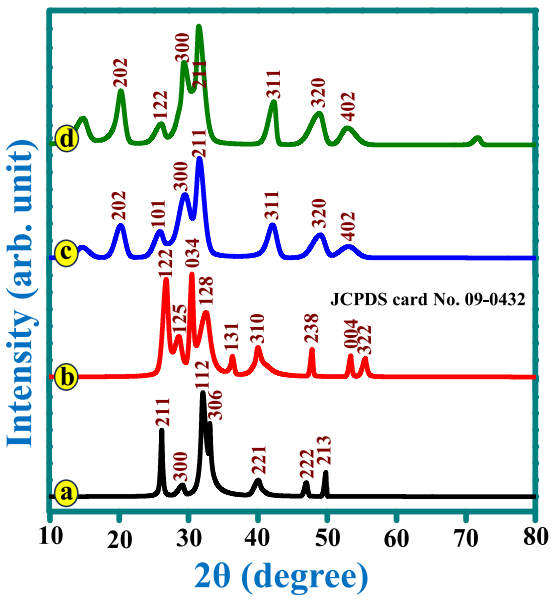

Fig. 3. XRD patterns of (**a**) HAP, (**b**) Ce-HAP, (**c**) Ce-HAP/CS, and (**d**) Ce-HAP/CS/BF nanocomposite.

2θ = 16.2°, 21.19°, 34.14°, and 59.85°, attributed to bioactive glass (BF). These are present alongside characteristic Ce-HAP and CS peaks. The indexed planes include (202), (122), (300), (211), (311), (320), and (402), validating the incorporation of BF into the composite. The absence of any new or unidentified peaks confirms that no additional or intermediate phases were formed during the composite fabrication. This confirms the successful integration of all constituents into a structurally coherent composite, ensuring phase purity and the potential for enhanced functional properties suitable for biomedical applications.

3.3. Morphological analysis

Fig. 4 (a-d) revealed the HRSEM micrographs illustrating the synthesized HAP, Ce-HAP, Ce-HAP/CS, and Ce-HAP/CS/BF nanocomposites. Fig. 4(a) displays the synthesized HAP sample, which exhibits a grain-shaped microstructure. The observed micrographic image reveals the formation of dense, structured topography with a macro porous structure. The HAP structure reveals the formation of a uniform microstructure without secondary particle formation. Furthermore, according to Fig. 4b), the Ce incorporation into the HAP leads to the production of spherical-like morphology. Additionally, the structure of the Ce-HAP/CS nanocomposites depicted in Fig. 4 (c) shows the creation of an aggregated surface structure, which could be the result of the Ce-HAP matrix integration in CS. The surface texture of the Ce-HAP/CS/BF is shown in Fig. 4(d). Examining the porous microstructure in the

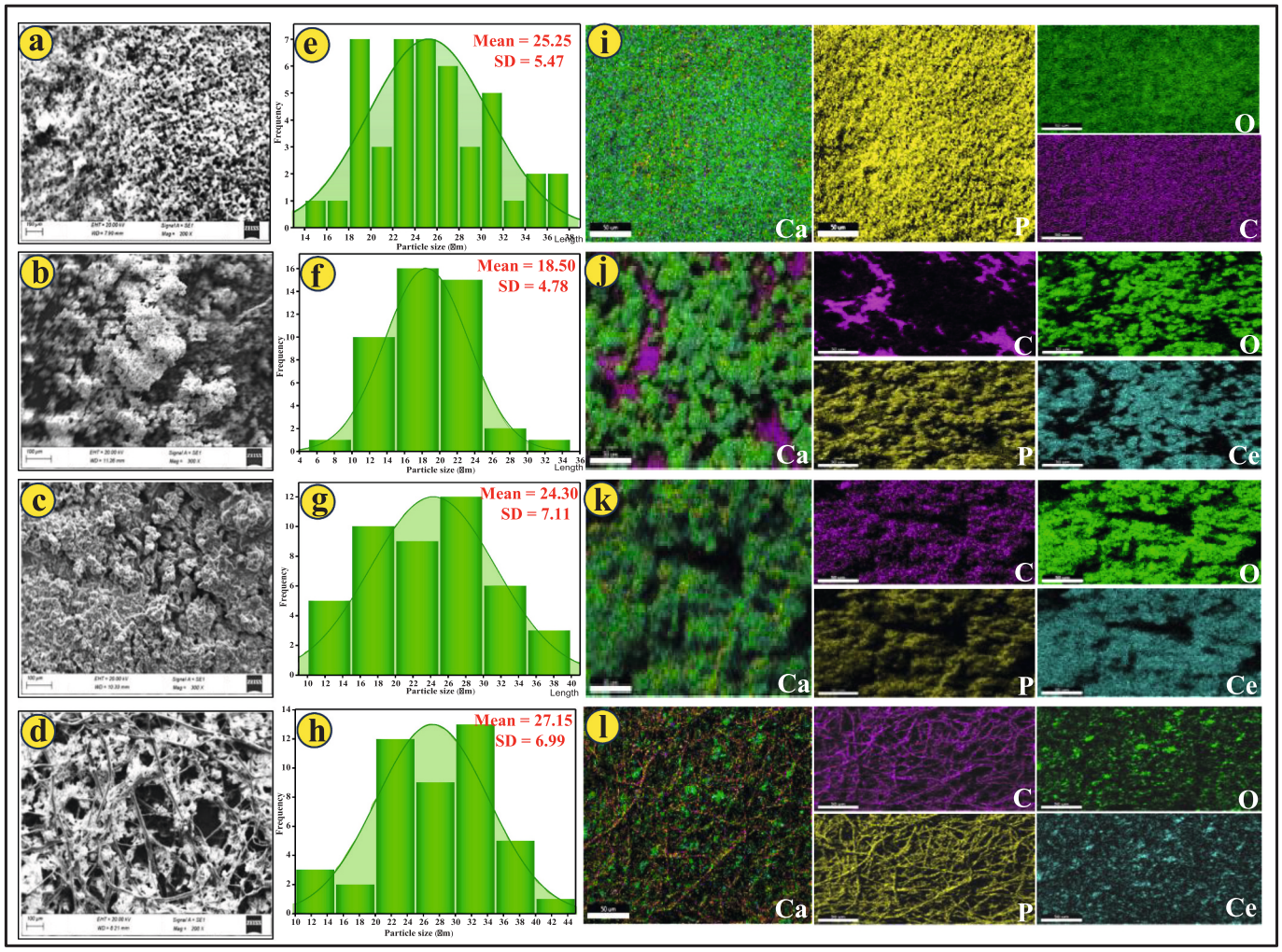

Fig. 4. (**a-d**) FESEM images; (**e-h**) histograms showing the particle size distribution of HAP, Ce-HAP, Ce-HAP/CS, and Ce-HAP/CS/BF; and (**i-l**) elemental mapping images showing the distribution of individual elements Ca, P, O, C, and Ce.

Ce-HAP/CS material, it can be observed that the composite has a homogeneous distribution in solid structure exhibiting an arrangement matching fibres. Comparable porous microscopy images for the Ce-HA/CS/BF materials were successfully acquired. Accordingly, the HRSEM observations demonstrated that the material is extremely porous and has excellent interrelationships which makes it advantageous enabling the adherence of various contamination as well as for the absorption of organic and inorganic materials from the aqueous environment. The average particle size of the materials was calculated based on their distribution, as presented in the histograms and corresponding micrographs depicted in Fig. 4 (e- h). Fig. 4(i- l) illustrate the detailed particle size distribution and morphology, offering insight into the variations and uniformity across samples. Further, the mapping analysis confirms that the elements are evenly distributed in the structure, which confirms the nanocomposite indicates the presence of Ca, P, O, Ce, and C and does not exhibit any additional elements in its structure. Fig. 5 displays the EDAX spectra and quantitative elemental composition for (a) HAP, (b) Ce-HAP, (c) Ce-HAP/CS, and (d) Ce-HAP/CS/BF nanocomposite, confirming the presence and distribution of key elements in each sample. In the spectrum of pure HAP (Fig. 5 a), the detected elements include calcium (Ca), phosphorus (P), oxygen (O), and carbon (C). The corresponding elemental composition is C (15.43 wt%, 19.07 at.%), O (41.32 wt%, 51.31 at.%), P (16.55 wt%, 14.40 at.%), and Ca (26.70 wt%, 15.22 at.%). These values are consistent with the expected stoichiometry of hydroxyapatite and indicate successful synthesis.

Following cerium incorporation (Fig. 5b), the Ce-HAP sample shows a new peak for cerium (Ce), with an elemental composition of C (11.2 wt %, 18.88 at.%), O (47.02 wt%, 59.5 at.%), P (12.1 wt%, 7.91 at.%), Ca

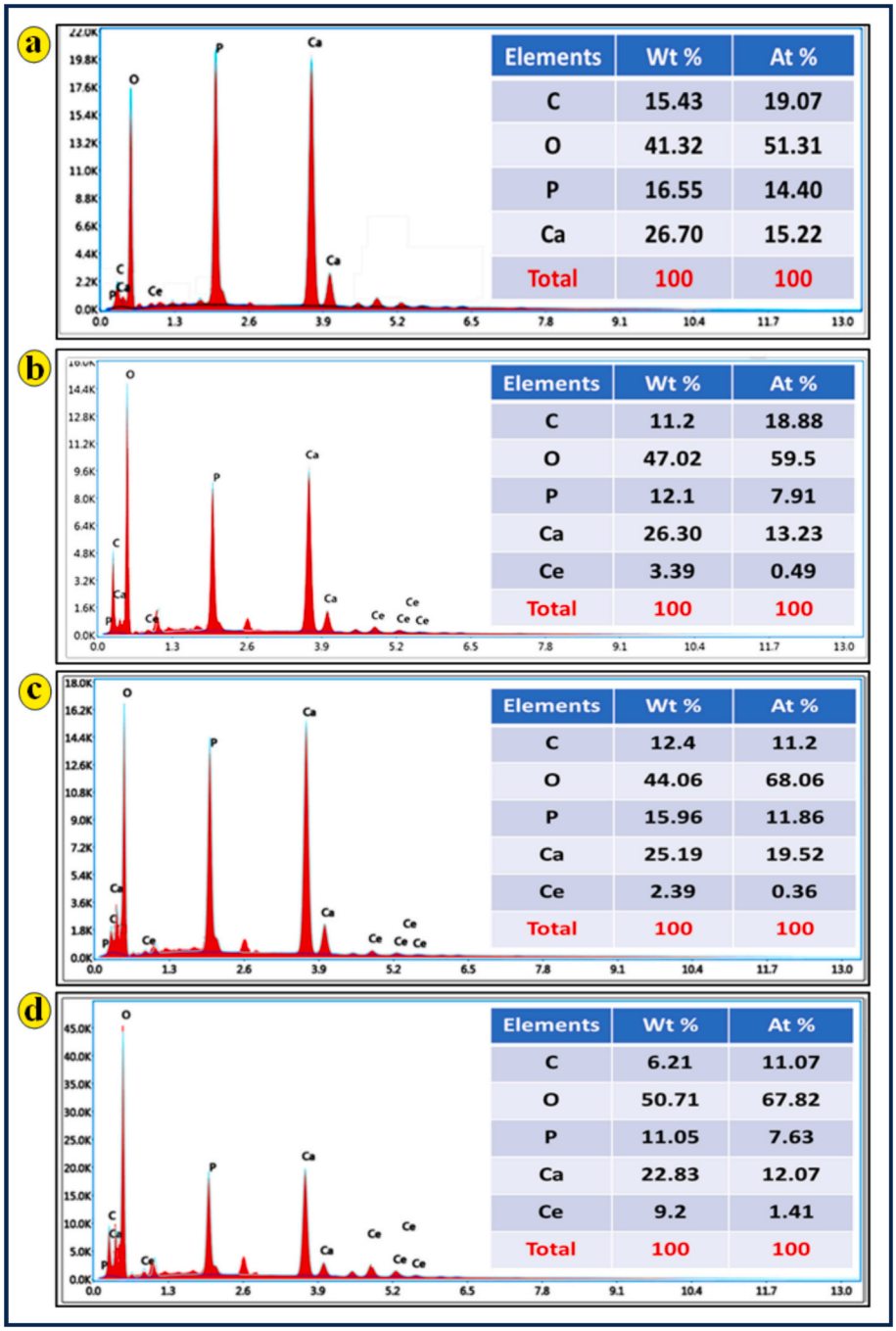

Fig. 5. EDAX spectra of (**a**) HAP, (**b**) Ce-HAP, (**c**) Ce-HAP/CS, and (**d**) Ce-HAP/CS/BF nanocomposite.

(26.30 wt%, 13.23 at.%), and Ce (3.39 wt%, 0.49 at.%). The detection of Ce confirms its successful doping into the HAP lattice. A noticeable increase in oxygen content and a slight reduction in phosphorus and carbon suggest potential formation of cerium oxides or Ce-substituted HAP. For the Ce-HAP/CS composite (Fig. 5c), the elemental composition is C (12.4 wt%, 11.2 at.%), O (44.06 wt%, 68.06 at.%), P (15.96 wt %, 11.86 at.%), Ca (25.19 wt%, 19.52 at.%), and Ce (2.39 wt%, 0.36 at. %). The presence of Ce is still evident, although in slightly lower concentration compared to Ce-HAP, indicating a more dispersed distribution. The moderate increase in C content is indicative of the chitosan (CS) matrix, while P and Ca remain within a similar range. In the Ce-HAP/CS/BF nanocomposite (Fig. 5d), the elemental analysis reveals C (6.21 wt%, 11.07 at.%), O (50.71 wt%, 67.82 at.%), P (11.05 wt%, 7.63 at.%), Ca (22.83 wt%, 12.07 at.%), and Ce (9.2 wt%, 1.41 at.%). A significant increase in Ce content compared to previous samples confirms effective loading of cerium within the composite. The elevated oxygen level and reduced carbon may be attributed to the inclusion of bioactive fiber (BF), which likely enhances oxygen-rich functional groups in the matrix. Overall, the EDAX spectra and elemental data confirm the stepwise incorporation of cerium, chitosan, and bioactive fiber into the HAP framework. Each modification results in characteristic shifts in elemental composition, validating the successful fabrication of the desired nanocomposite systems.

The HAP, Ce-HAP, and Ce-HAP/CS/BF were evaluated for the shape and size by the TEM micrograph, as shown in Fig. 5. The as-derived HAP from the biowaste materials exhibits a spherical structure formation with the approximate size of 200 nm Fig. 6 (a). Further, the HAP shown in Fig. 6 (b) confirms the incorporation of Ce atom in the HAP structure. The substitution of Ce in the HAP structure does not show any morphological changes. The Ce-HAP/CS/BF nanocomposite exhibited in Fig. 6 (c) indicates the formation of cluster-like morphology with maximum aggregation. The incorporation of CS and BF in the Ce-HAP structure reveals the formation of an aggregated structure, which is due to the moisture content present in the polymer and fiber structure. Fig. 6 (d) indicates the SAED pattern of the Ce-HAP/CS/BF nanocomposite, and this pattern demonstrates the highly oriented hexagonal crystal structure formation, which is in good agreement with the XRD investigations.

3.4. Thermal analysis

Thermogravimetric analysis (TGA) and differential thermal analysis (DTA) were performed to investigate the thermal stability and decomposition behaviour of the Ce-HAP/CS/BF nanocomposite, as shown in Fig. 7. The TGA curve (red) reveals a multi-step weight loss profile indicative of various decomposition events. Initially, a minor weight loss (2–3 %) occurs up to approximately 150 °C, which is attributed to the evaporation of adsorbed moisture. This is followed by a gradual weight loss between 150 °C and 300 °C, corresponding to the thermal degradation of the chitosan (CS) matrix and partial loss of organic content. A

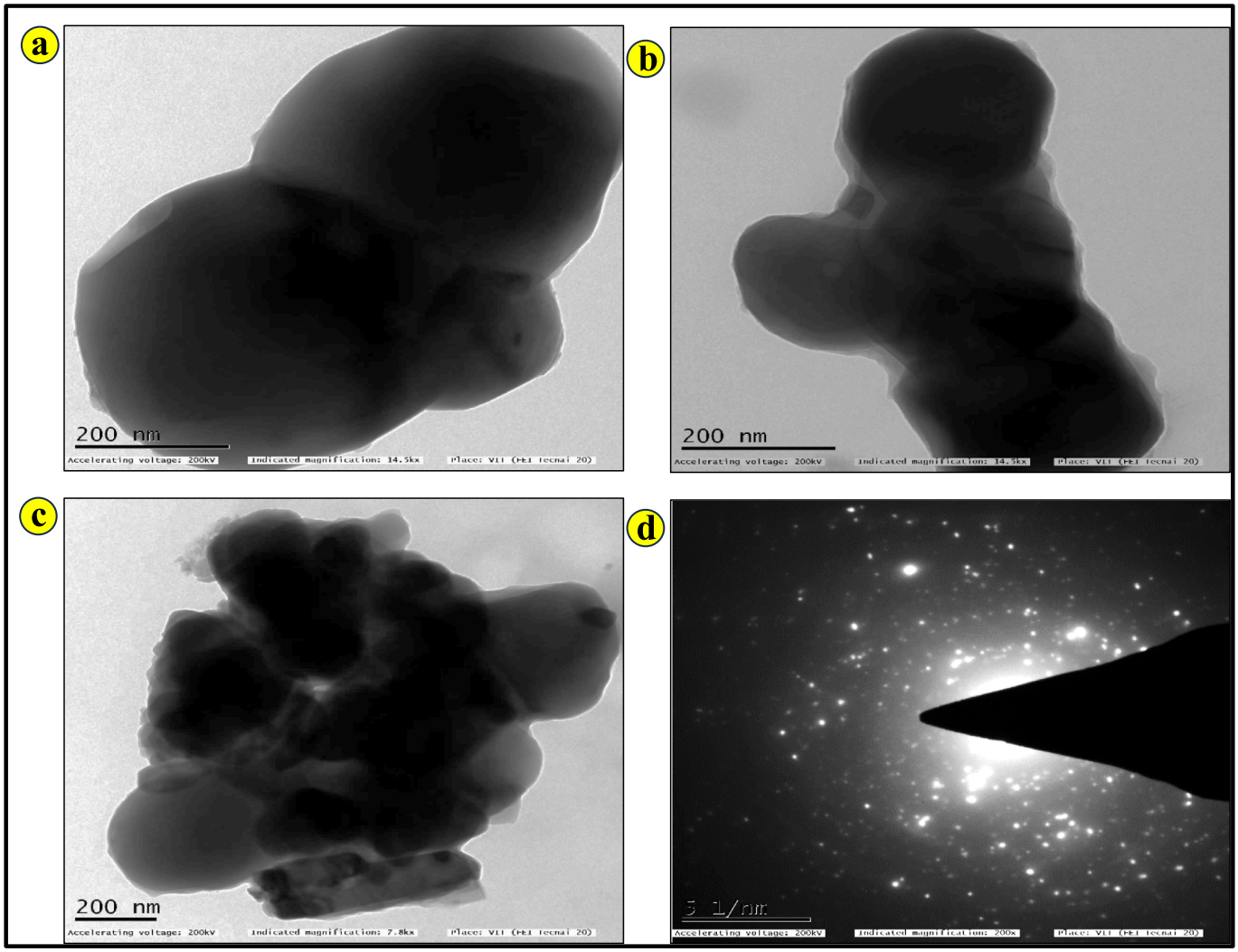

Fig. 6. TEM image of (**a**) HAP, (**b**) Ce-HAP, and (**c**) Ce-HAP/CS/BF nanocomposites and (**d**) SAED pattern.

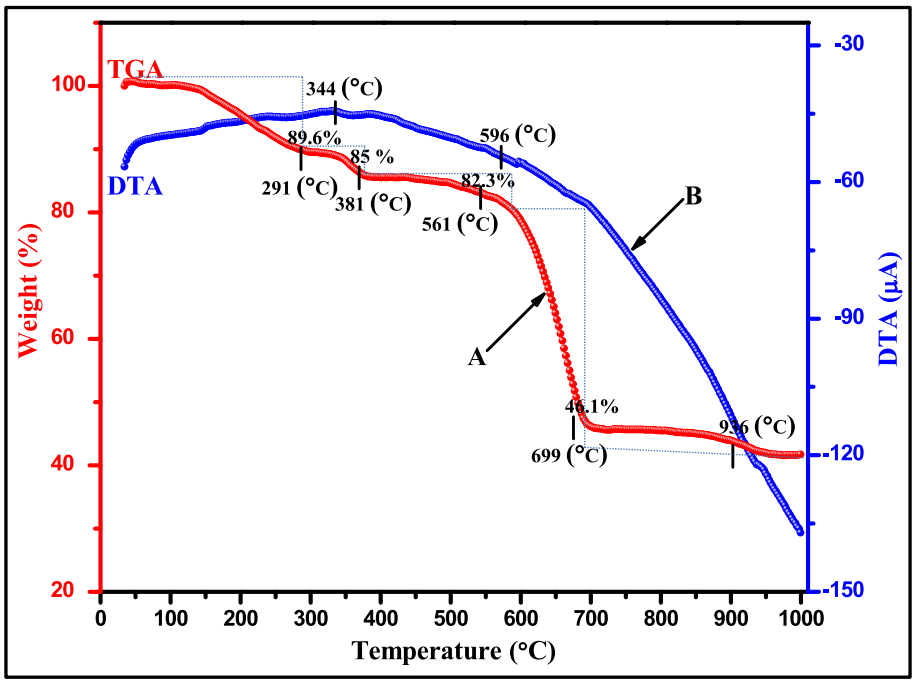

Fig. 7. TGA and DTA spectra of Ce-HAP/CS/BF nanocomposite.

more pronounced weight loss (30 %) is observed between 300 °C and 500 °C, which is attributed to the decomposition of chitosan and other organic moieties, including residual solvents or unreacted components. Beyond 500 °C, a significant weight loss continues, reaching a plateau around 600–700 °C, suggesting the breakdown of remaining organic fractions and potential phase transitions involving Ce-HAP or Bambo fiber constituents. The final residue at temperatures above 700 °C remains stable, indicating the formation of thermally stable inorganic phases, likely comprising Ce-HAP and boron-rich materials. The DTA curve (blue) complements the TGA data, exhibiting endothermic and exothermic peaks associated with phase transitions and decomposition reactions. An endothermic peak around 100–150 °C correlates with water loss, while exothermic events between 300 °C and 600 °C correspond to the degradation of organic components and potential crystallization or restructuring within the composite. The thermal stability of the nanocomposite, evidenced by a significant residual mass (40 %), confirms its suitability for applications requiring thermal endurance, such as biomedical implants or catalytic supports.

3.5. ICP-OES analysis for metal ion leaching assessment

To assess the compositional stability and environmental safety of the synthesized nanocomposites during repeated photocatalytic cycles, inductively coupled plasma optical emission spectrometry (ICP-OES) was employed to detect possible leaching of constituent ions (Ca^{2+}, P^{5+}, Ce^{3+}, and trace elements) into the aqueous medium. The HAP, Ce-HAP, Ce-HAP/CS, and Ce-HAP/CS/BF samples were subjected to five consecutive photocatalytic degradation cycles, and the post-reaction solutions were analyzed (Table 1).

Table 1
ICP-OES results showing Ce ion concentration (ppm) in the solution after each photocatalytic cycle.

Cycle number	Ca (ppm)	P (ppm)	Ce (ppm)
1	0.91 ± 0.01	0.76 ± 0.12	0.43 ± 0.03
2	0.88 ± 0.02	0.73 ± 0.04	0.37 ± 0.02
3	0.86 ± 0.13	0.75 ± 0.22	0.40 ± 0.12
4	0.85 ± 0.12	0.73 ± 0.03	0.39 ± 0.02
5	0.81 ± 0.21	0.72 ± 0.02	0.36 ± 0.03

Across all cycles, the detected Ca, P, and Ce concentrations remained far below their respective WHO permissible limits. The minimal ion release (≤1 ppm for Ce and ≤ 1 ppm for Ca and P) suggests strong lattice stability of the hydroxyapatite phase and robust immobilization of Ce^{3+} ions within the crystal structure. The chitosan and bamboo fiber matrix further minimized surface dissolution by providing an additional organic protective layer. This low-leaching behaviour confirms that the composites maintain their chemical integrity during repeated photocatalytic operations, ensuring both reusability and environmental safety.

3.6. Antibacterial activity

To eradicate environmental infections from aqueous waterbodies, it is desirable to develop antibacterial materials. The as-synthesized HAP, Ce-HAP, Ce-HAP/CS, and Ce-HAP/CS/BF samples were tested for their antibacterial efficacy versus two pathogenic strains, particularly *S. aureus* and *E. coli,* which have been frequently employed to treat frequent environmental infections found in ecology. To examine the as-synthesized samples, Fig. 8 (i-ii) illustrates the zone of inhibition encompassing the as-prepared material at two distinct doses. The clear zone formation confirms that the prepared material resistance to the pathogenic like 50 and 100 mg/µL, over *S. aureus* and *E. coli.* For both the bacterial strains, it has been observed the formation of clear zones around the disc bacterial strains. The as-synthesized composite zones of inhibition for HAP, Ce-HAP, Ce-HAP/CS, and Ce-HAP/CS/BF are shown in the image. From the bacterial analysis, it has been clear that the higher concentration such as 100 µL also the composite Ce-HAP/CS/BF shows maximum inhibition zone. This indicates that the sample containing CS and BF in the Ce-HAP structure acts as a better antibacterial material for both bacterial strains. Furthermore, the results reveal that the Ce-HAP/CS/BF composite is more resistance to *E. coli* than *S. aureus.* The largest area of inhibition dimensions versus *E. coli* was ultimately determined by the Ce-HAP/CS/BF nanocomposites and was explained by the division in the bacterial cell membrane structure, which could be due to the attraction between the strains and nanocomposites. The antibacterial activity is proportional to the reactive oxygen species

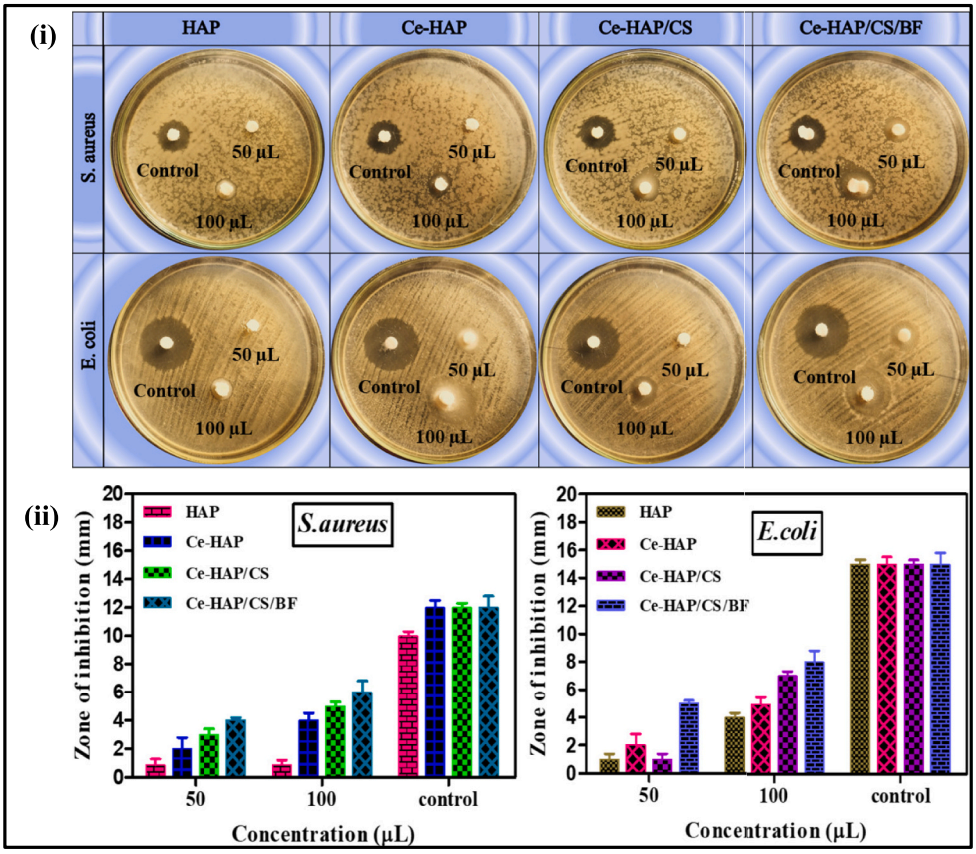

Fig. 8. (I) Photographs and (II) Bar diagram showing the antibacterial activity of HAP, Ce-HAP, Ce-HAP/CS, and Ce-HAP/CS/BF nanocomposites at 50 and 100 µL against *E. coli* and *S. aureus*.

(ROS), surface area, and size of the element. Fig. 9 depicts the antibacterial mechanism of the generated Ce-HAP/CS/BF nanocomposite. Nanocomposite photocatalysts can generate ROS such as $\bullet O_2^-$, ·OH, and H_2O_2 in the presence of dissolved O_2, which contributes to extra free radical production. The Ce-HAP/CS/BF nanocomposite generates ROS via the Fenton reaction, which causes DNA damage and protein denaturation, ultimately leading to the microorganism's death.

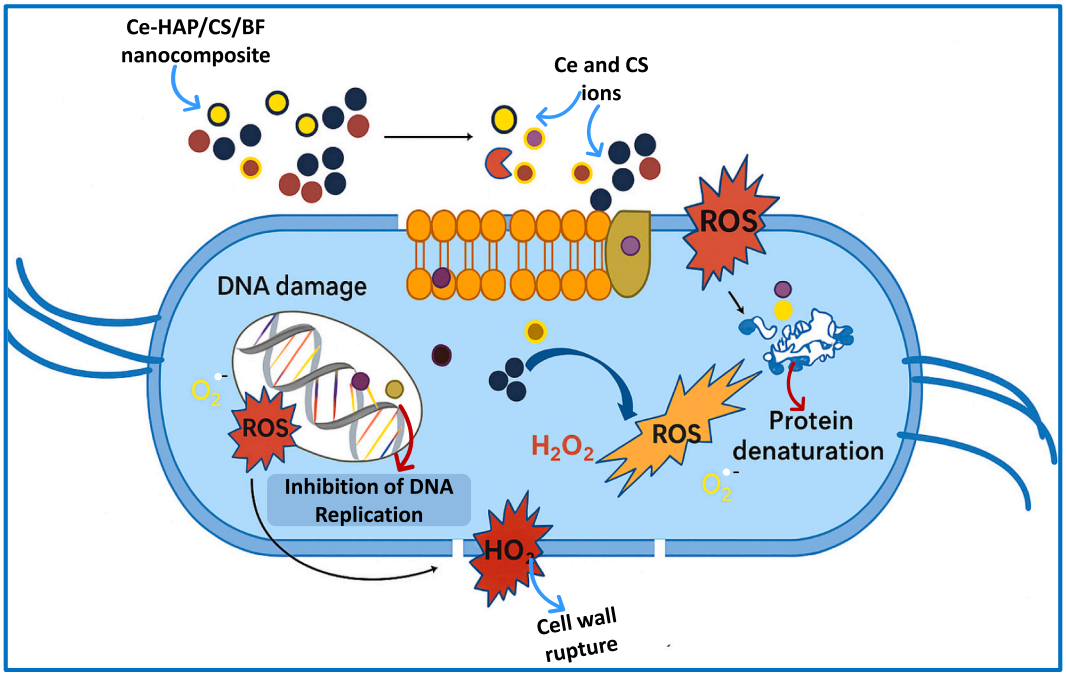

Fig. 9. Schematic possible mechanism of antibacterial activity of Ce-HAP/CS/BF nanocomposite.

3.7. MTT assay

The biocompatibility of the Ce-HA/CS/BF nanocomposite was assessed through in vitro cytotoxicity testing using MG63 osteoblast-like cells. Cell viability was evaluated after 5 days of incubation at varying concentrations of the composite (12.5, 25, 50, and 100 μg/mL), and the results are presented in Fig. 10. The optical microscopy images Fig. 10 (a-e) reveal morphological changes in cell populations with increasing composite concentrations, while the accompanying bar graph quantifies the percentage of viable cells relative to the untreated control. Fig. 10 (a) shows the control sample, where cells display elongated, spindle-shaped morphology and are densely populated, indicative of healthy, proliferating osteoblasts. Upon treatment with the Ce-HA/CS/BF composite at a low concentration of 12.5 μg/mL (Fig. 10b), slight changes in morphology and density were observed, though cell attachment and spreading remained adequate. At 25 μg/mL (Fig. 10c), cells appeared well-distributed with visible round and partially spread morphology, suggesting favourable interactions with the composite material. As the concentration increased to 50 μg/mL and 100 μg/mL (Fig. 10e), cells retained viable characteristics, although a minor reduction in density was observed at the highest concentration. However, no significant cytotoxic effects were noted, and the cell morphology remained generally intact. These observations are supported by the bar graph, which shows over 90 % viability for all tested concentrations, with the peak viability observed around 25–50 μg/mL. Importantly, even at 100 μg/mL, the viability remained above 85 %, confirming the low toxicity of the composite. The high cell viability across all concentrations can be attributed to the bioactive nature of the composite components. Cerium-substituted hydroxyapatite enhances cellular interactions, while chitosan provides a conducive matrix for cell adhesion and proliferation. The incorporation of BF likely contributes to mechanical reinforcement without compromising biocompatibility. Overall, the Ce-HA/CS/BF nanocomposite demonstrates excellent cytocompatibility, with minimal toxicity even at elevated concentrations. These results confirm the potential of this composite for bone tissue engineering applications, where biomaterials must promote osteoblast viability, proliferation, and differentiation for effective tissue regeneration.

3.8. Swelling and degradation behaviours in simulated body fluid (SBF)

The Fig. 11 (i) swelling ratios and Fig. 11 (ii) degradation behaviours of (a) HAP, (b) Ce-HAP, (c) Ce-HAP/CS, and (d) Ce-HAP/CS/BF composites at 0, 2, 4, 6, 8, 10, 12, and 14 days of immersion in SBF. The swelling and degradation behaviour of the synthesized samples HAP, Ce-HAP, Ce-HAP/CS, and Ce-HAP/CS/BF were investigated in vitro by immersing each sample in simulated body fluid (SBF) over 14 days. The experiments were conducted at specific time intervals (0, 2, 4, 6, 8, 10, 12, and 14 days), and the corresponding results are presented in Fig. 11 (i-ii).

3.8.1. Swelling behaviour

As depicted in Fig. 11 (i), the swelling ratio of all samples gradually increased with time. The swelling percentage was calculated using the following equation:

$$\text{Swelling ratio } (\%) = \frac{W_w - W_d}{W_d} \times 100 \quad (1)$$

where Ww is the wet weight and Wd is the dry weight of the sample after immersion.

The results clearly indicate that the swelling percentage increased progressively with immersion time, reaching 31.7 % for (a) HAP, 38.9 % for (b) Ce-HAP, 51.9 % for (c) Ce-HAP/CS, and 61.8 % for (d) Ce-HAP/CS/BF composite after 14 days in SBF solution. Among all tested compositions, the Ce-HAP/CS/BF composite exhibited the highest swelling capacity throughout the 14-day immersion period. This enhanced swelling behaviour can be attributed to the hydrophilic nature of chitosan and the highly porous structure introduced by the boron fiber reinforcement. Similarly, the Ce-HAP/CS/BF composite showed improved swelling compared to Ce-HAP and pure HAP, highlighting the synergistic effect of the polymer and fiber in facilitating water absorption. In contrast, pure HAP and Ce-HAP demonstrated lower swelling percentages, likely due to their dense, crystalline microstructure, which restricts fluid penetration.

3.8.2. Degradation behaviour

The degradation profiles of the samples in SBF are shown in Fig. 11 (ii) and were calculated using the formula:

$$\text{Degradation } (\%) = \frac{W_d}{W_0} \times 100 \quad (2)$$

where W_0W₀ is the initial dry weight of the sample and Wd is the dry weight after immersion.

The results revealed a progressive decline in sample weight over time, indicating ongoing degradation for all formulations. The results clearly indicate that the degradation percentage increased to 38.1 % for (a) HAP, 48.9 % for (b) Ce-HAP, 61.1 % for (c) Ce-HAP/CS, and 68.3 %

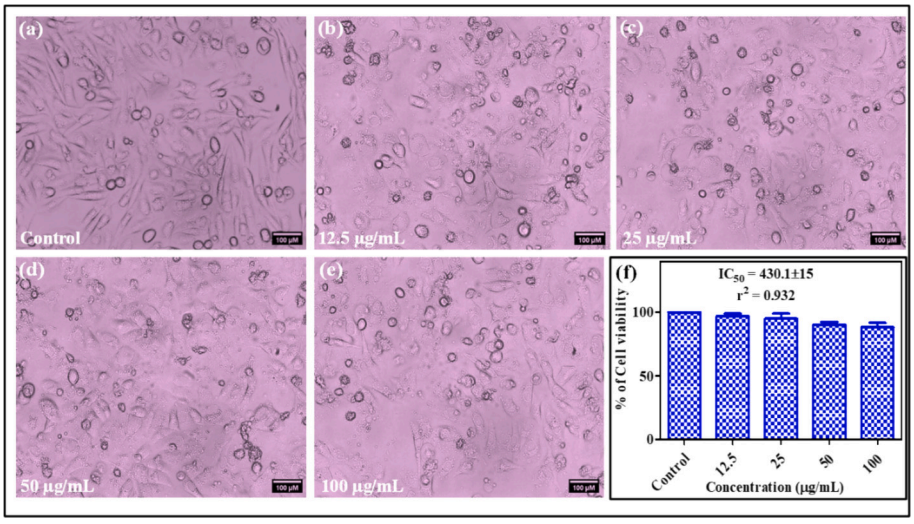

Fig. 10. Cell viability (%), and optical images for the cell viability of Ce-HA/CS/BF composite at different concentrations (**a**) Control, (**b**) 12.5 μL, (**c**) 25 μL, (**d**) 50 μL, and (**e**) 100 μL at 5 days of incubation.

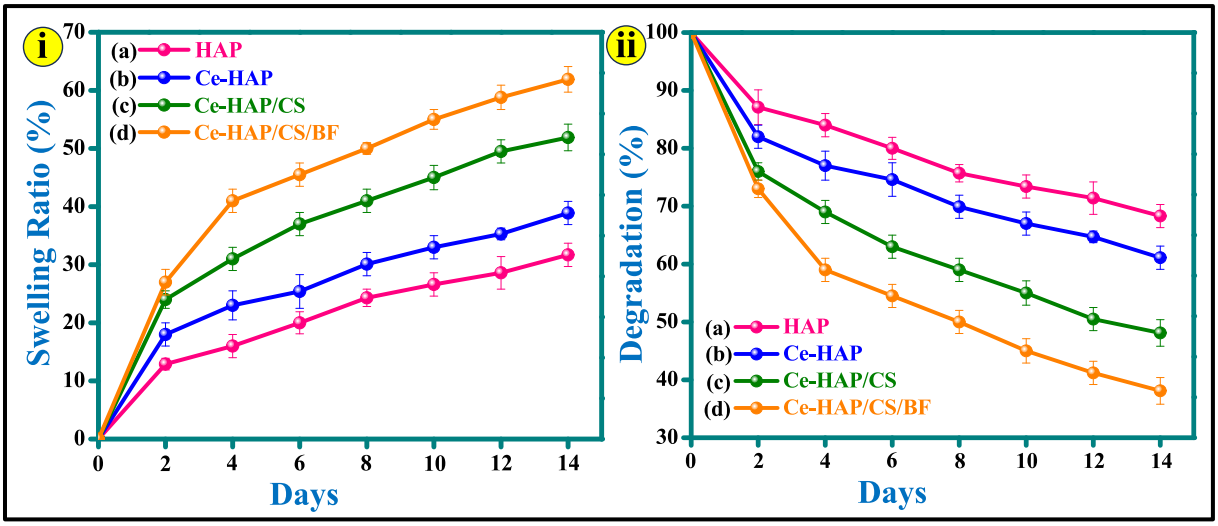

Fig. 11. (**i**) Swelling ratios, (**ii**) degradation behaviours of (**a**) HAP, (**b**) Ce-HAP, (**c**) Ce-HAP/CS, and (**d**) Ce-HAP/CS/BF Composite at 0, 2, 4, 6, 8, 10, 12 and 14 days of immersion in SBF.

for (d) Ce-HAP/CS/BF composite after 14 days of immersion in SBF solution. However, the rate of degradation varied depending on the composition. The degradation rate, followed by the Ce-HAP/CS/BF composite, suggests enhanced structural integrity and slower degradation in the presence of both CS and BF. This improved stability can be attributed to the formation of a robust CS polymer–ceramic-fiber matrix, which resists rapid disintegration in physiological conditions. On the other hand, pure HAP and Ce-HAP showed higher degradation rates, which may be due to their lack of polymeric and fibrous reinforcement, making them more prone to ionic dissolution in the SBF medium. The swelling and degradation studies demonstrate that the Ce-HAP/CS/BF composites, at BF content, exhibit optimal behaviour for biomedical applications. High swelling ratios ensure good fluid absorption and biological interaction, while controlled degradation ensures mechanical integrity over a suitable time frame for bone regeneration. These properties affirm the potential of Ce-HAP/CS/BF composites as promising scaffolds for bone tissue engineering.

3.9. UV-DRS analysis

The UV–vis DRS analysis was used to assess the optical properties and bandgap characteristics of HAP, Ce-HAP, Ce-HAP/CS, and Ce-HAP/CS/BF nanocomposites. From the UV–Vis absorption spectra Fig. 12(a). the pristine HAP exhibits the lowest absorbance, whereas the incorporation of cerium (Ce) significantly enhances the absorbance in the visible region, as observed with the Ce-HAP sample. This enhancement can be ascribed to the introduced Ce in the HAP lattice, which creates new energy levels in the bandgap that allow for more light absorption. When chitosan (CS) is combined with Ce-HAP (Ce-HAP/CS), a further enhancement in absorbance is observed [45]. As a biopolymer, chitosan may improve Ce-HAP particle dispersion, hence raising the effective surface area exposed to light. The Ce-HAP/CS/BF nanocomposite exhibits the highest absorbance, indicating a potential synergistic interaction between CS, and BF likely offers a scaffold that not only improves the dispersion of Ce-HAP particles but also may introduce additional light-absorbing sites due to their organic nature. The bandgap energy (Eg) was calculated using Tauc plot equation and the results are shown in Fig. 12(b). [46]

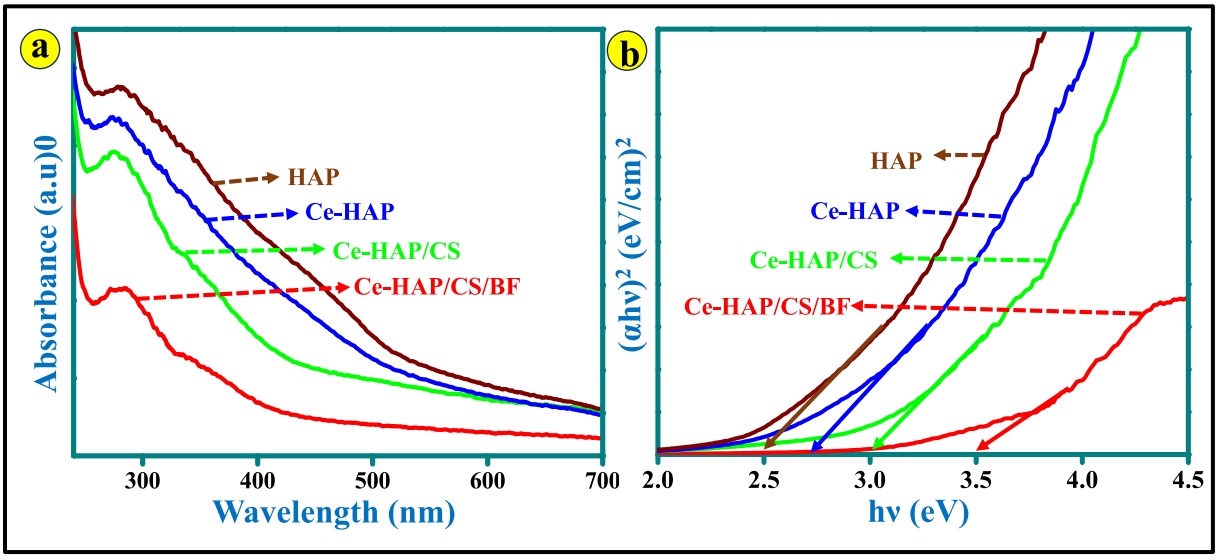

Fig. 12. (**a**) Absorption spectra and (**b**) Tauc plots of HAP, Ce-HAP, Ce-HAP/CS, and Ce-HAP/CS/BF nanocomposite.

$$(\alpha h\nu) = A(h\nu - Eg)_{n/2} \quad (3)$$

where α signifies the absorption coefficient, h denotes the Planck constant, and ν represents light frequency, with A as a constant. The estimated bandgap values for HAP, Ce-HAP, Ce-HAP/CS, and Ce-HAP/CS/BF are 2.56, 2.72, 3.02 and 3.53 eV, respectively. By adding BF and CS, the bandgap can be reduced, improving the material's capacity to absorb visible light. The bandgap decrease can be described by the emergence of new electronic states in the band structure, which are brought about by the substitution of cerium and organic components.

3.10. X-ray photoelectron spectroscopy (XPS) analysis

The XPS was employed to investigate the surface chemical composition and oxidation states of the constituent elements in the Ce-HAP/CS/BF nanocomposite. The analysis was carried out using a high-

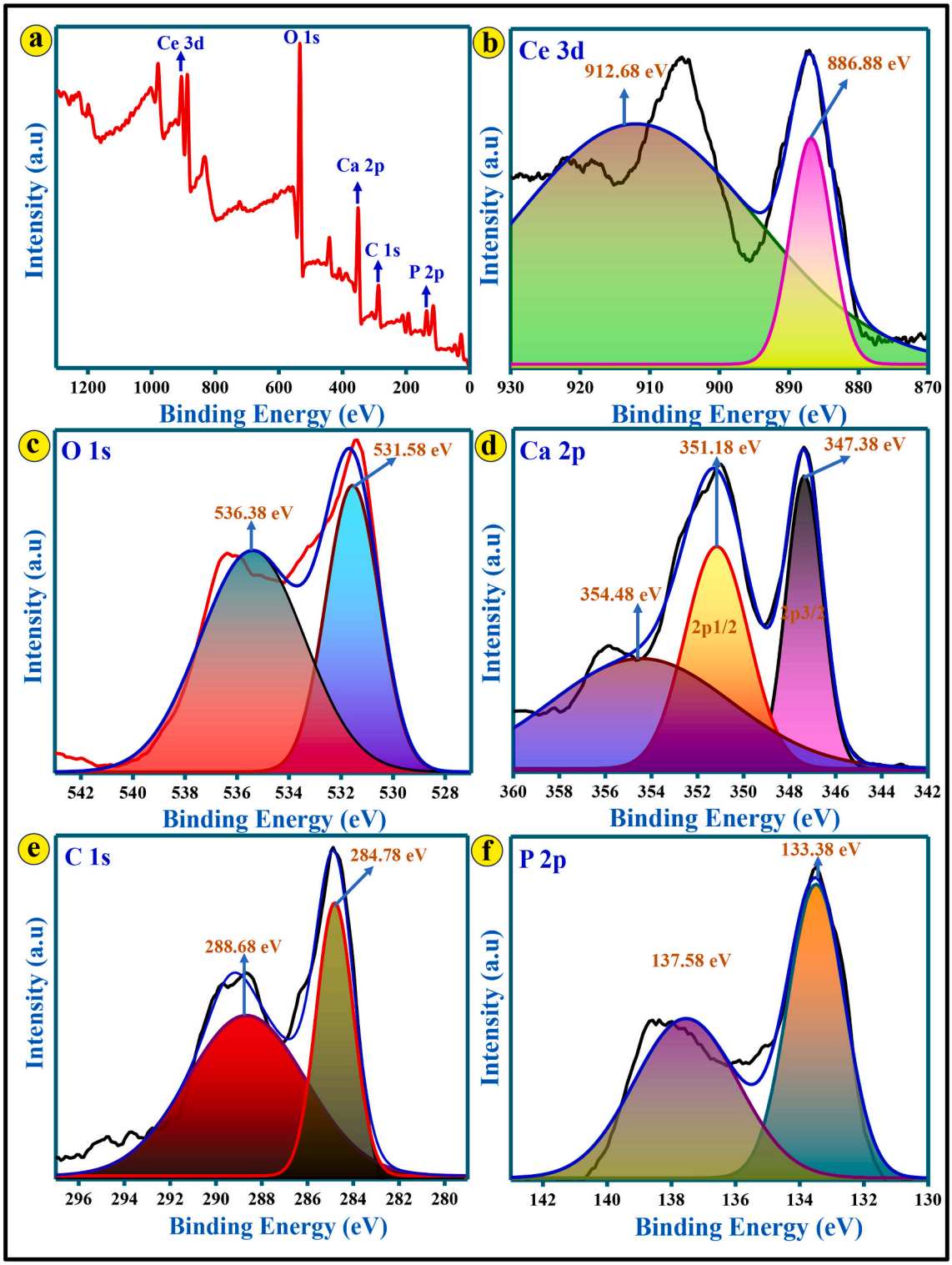

Fig. 13. XPS spectra of (a) survey scan spectra of Ce-HAP/CS/BF nanocomposite and high-resolution spectra of (b) Ce 3d, (c) O 1 s, (d) Ca 2p, (e) C 1 s, and (f) p 2p.

resolution XPS system equipped with a monochromatic Al Kα radiation source (hν = 1486.6 eV). The spectra were collected in an ultra-high vacuum chamber under a base pressure of ~10^{9} mbar. The binding energies (BEs) were calibrated against the C 1 s peak at 284.6 eV, corresponding to adventitious carbon, to correct for any charge shifting. Fig. 13 (a) shows the survey scan spectrum, which reveals the presence of characteristic peaks corresponding to cerium (Ce), calcium (Ca), phosphorus (P), oxygen (O), and carbon (C), confirming the successful incorporation of all expected elements in the Ce-HAP/CS/BF composite system. No significant signals from contaminants or impurities were observed, indicating high surface purity. High-resolution deconvoluted spectra were further analyzed for the following core levels. Fig. 13 (b) showing the Ce 3d Spectrum: The Ce 3d region exhibits multiple spin-orbit split peaks, typical of mixed oxidation states Ce^{3+} and Ce^{4+}. The spectrum shows prominent peaks assigned to Ce $3d_{5/2}$ and Ce $3d_{3/2}$, with distinct multiplet splitting, indicating the coexistence of Ce^{4+} (CeO_2-like environment) and Ce^{3+} (Ce_2O_3-like features). The complex nature of the Ce 3d spectrum is consistent with surface oxygen vacancies and redox activity, which are beneficial for catalytic and biological performance. The relative Ce^{3+} content, determined by the ratio of Ce^{3+} to total Ce^{3+} and Ce^{4+} peak areas, was 18.5 % for the nanocomposite, higher than that of pristine CeO_2 NPs (13.1 %). This higher Ce^{3+}

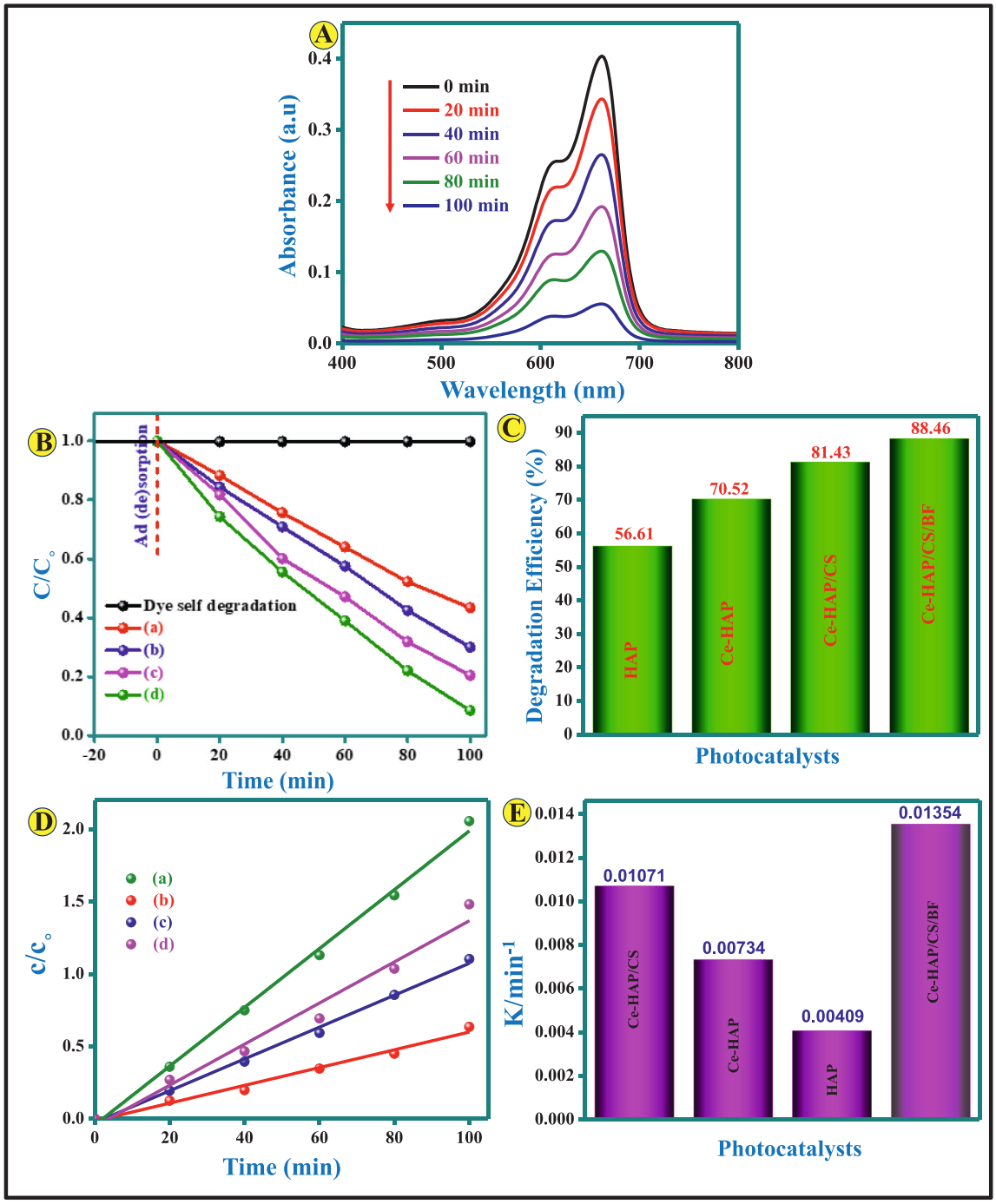

Fig. 14. (**a**) Photocatalytic performance of Ce-HAP/CS/BF nanocomposite evaluated against MB dye, (**b**) Photocatalytic performance, (**c**) Degradation efficiency, and (**d**) Pseudo first order kinetic model, and (**e**) rate constant of Ce-HAP/CS/BF nanocomposite for MB dye degradation under UV–visible light irradiation (**a-** HAP, **b-** Ce-HAP, **c-** Ce-HAP/CS, **d-**Ce-HAP/CS/BF).

concentration, along with the associated oxygen vacancies, plays a critical role in enhancing photocatalytic activity. Ce^{3+} species act as electron traps, suppressing the recombination of photogenerated electron–hole pairs, while oxygen vacancies promote the adsorption and activation of oxygen molecules. These trapped electrons generate superoxide radicals ($^{\bullet}O_2^-$), and photogenerated holes form hydroxyl radicals ($^{\bullet}OH$), both of which actively degrade methylene blue. Moreover, the Ce^{3+}/Ce^{4+} redox cycle sustains dynamic charge transfer, prolonging carrier lifetimes and maintaining efficient photocatalysis, which explains the superior performance of the Ce-HAP/CS/BF composite compared to pure CeO_2.

Fig. 13 (c) exhibited the O 1 s Spectrum: The O 1 s peak is deconvoluted into three components: the first at ~530.0 eV corresponds to lattice oxygen in metal oxides (Ce—O and Ca—O bonds), the second at ~531.6 eV is attributed to surface hydroxyl groups or chemisorbed oxygen species, and the third component at ~533.1 eV is associated with adsorbed water or organic oxygen species. The presence of hydroxylated surfaces can promote enhanced biocompatibility and cell interactions. Fig. 13 (d) presented in the Ca 2p Spectrum: The Ca 2p region shows two clear peaks at ~347.2 eV (Ca $2p_{3/2}$) and ~ 350.7 eV (Ca $2p_{1/2}$), which are characteristic of divalent calcium in hydroxyapatite. The peak separation of ~3.5 eV and symmetric peak shapes confirm the chemical integrity of the calcium environment in the HAP lattice. Fig. 13 (e) showed the C 1 s Spectrum: The carbon spectrum shows multiple components: the dominant peak at ~284.6 eV is attributed to C–C/C=C bonding from the chitosan matrix and adventitious carbon; a second peak at ~286.2 eV corresponds to C—O or C–OH functional groups; and a third peak around ~288.5 eV is related to O=C–O species, indicating carboxyl or ester groups. These functionalities are essential for cross-linking and bio-interaction within the chitosan matrix. Fig. 13(f) revealed the P 2p Spectrum: The phosphorus region reveals two peaks located at ~133.2 eV and ~ 134.1 eV, corresponding to P $2p_{3/2}$ and P $2p_{1/2}$, respectively, confirming the presence of phosphate groups (PO_4^{3-}) in the HAP structure. The narrow peak width and binding energy values affirm the structural stability of the phosphate lattice in the hybrid. The XPS results collectively validate the successful synthesis of the Ce-HAP/CS/BF nanocomposite and confirm the expected oxidation states and chemical bonding environments for each element, reinforcing the structural and functional integration of the hybrid system.

3.11. Photocatalytic degradation test

The photocatalytic activity of the prepared photocatalyst was evaluated through the degradation of the MB dye solution under visible light in a photocatalytic glass reactor (Fig. 14.a-e). In typical experiments, 50 mg of the catalyst was dispersed in 100 mL of MB dye solution (10 mg/L) within the reaction vessel. The suspension was magnetically stirred in the dark for 20 min under ambient conditions to ensure equilibrium adsorption before illumination. Following this, the mixture was exposed to visible light. Following this, the mixture was exposed to visible light from a 300 W Xe lamp ($\lambda > 420$ nm), with the light intensity at the reaction surface measured to be 100 mW cm^{-2} using a calibrated optical power meter. During the reaction, aliquots of 3 mL were withdrawn at 20 min intervals, and the sample was separated from the mixture via filtration. The concentration of MB in the solution was determined by measuring its absorbance at 664 nm using UV–vis absorption spectroscopy. All photocatalytic degradation tests were performed in triplicate to ensure reproducibility. The degradation efficiency of MB was calculated using Eq. (4):

$$\textit{Degradation efficiency}\ (\%) = \frac{C_0 - C_t}{C_0} \tag{4}$$

where C_0 and C_t represent the initial and final concentrations of the MB dye solution, respectively. To identify the primary reactive species involved in the photocatalytic degradation process, radical scavenger tests were conducted. Four free-radical trapping agents were employed: ammonium oxalate (AO, 1 mmol), benzoquinone (BQ, 0.2 mmol), isopropanol (IPA, 1 mL), and silver nitrate ($AgNO_3$, 1 mmol). These agents were used to quantitatively determine the contributions of different active species generated during the photocatalytic degradation process.

3.11.1. Degradation efficiency analysis

The photocatalytic performance of the synthesized materials was assessed by monitoring the degradation of MB under visible-light irradiation. As shown in Fig. 15 (a), the control experiments conducted using light alone (in the absence of a catalyst) or catalysts alone (in the absence of light) resulted in negligible degradation of MB during the test period, confirming that the synergistic effect of both the catalyst and photon energy is essential for effective MB degradation. The pristine HAP photocatalyst demonstrated limited photocatalytic activity, achieving 41 % MB degradation after 100 min. In comparison, Ce-HAP photocatalysts showed a degradation rate of 29.56 %. Notably, the Ce-HAP/CS/BF composite system exhibited superior photocatalytic efficiency, achieving an 88 % degradation rate under identical conditions. The temporal evolution of the UV–vis absorption spectra of the MB solution during the reaction is presented in Fig. 15 (d). The characteristic absorption peak of MB gradually diminished, reaching its minimum intensity after 100 min of visible-light irradiation, indicating effective degradation by the Ce-HAP/CS composite. The kinetics of MB photocatalytic degradation were analyzed by fitting the experimental data to a pseudo-first-order model, as described by Eq. (5):

$$-\ln\left(\frac{C_0}{C_t}\right) = kt \tag{5}$$

where C_0 and C_t are the initial and final concentration of MB at time t (min), and k is the pseudo-first-order rate constant(min^{-1}). The linear regression analysis revealed a strong correlation with the pseudo-first-order model, with regression coefficients (R^2) exceeding 0.95 (Table 2). The calculated rate constants were 0.047, 0.11, and 0.689 min for pristine HAP, Ce-HAP, Ce-HAP/CS/ and Ce-HAP/CS/BF photocatalysts, respectively (Fig. 15b). Notably, the Ce-HAP/CS/BF composite exhibited the highest rate constant, approximately 10-fold and 3-fold greater than those of pristine HAP, Ce-HAP, Ce-HAP/CS, and Ce-HAP/CS/BF, respectively. The enhanced photocatalytic degradation

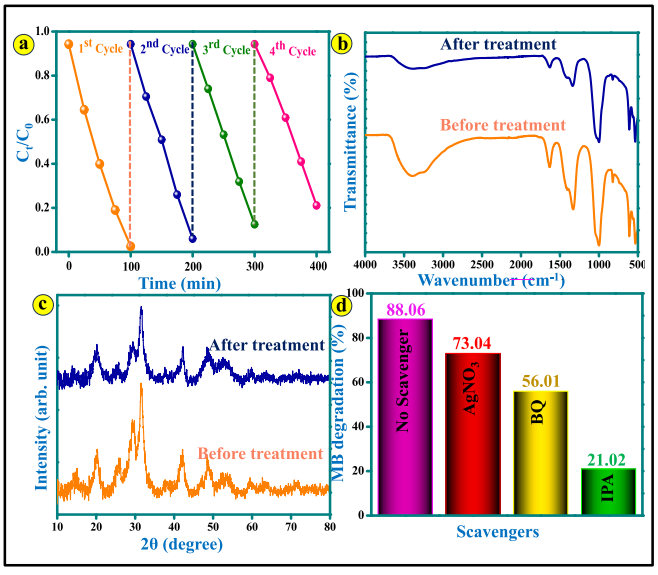

Fig. 15. (**a**) Recycling use. (**b**) FTIR spectra and (**c**) XRD patterns of Ce-HAP/CS/BF nanocomposite for MB degradation after the 4th cycle. (d) Impacts in the photocatalytic degradation of MB dye with Ce-HAP/CS/BF photocatalyst of various quenchers.

Table 2
Efficiency, K_{app}, R^2 values of the as-prepared samples.

S. no	Sample	Efficiency (%)	K_{app} (min^{-1})	(R^2)
		MB	MB	MB
1	HAP	56.61	0.00409	0.9831
2	Ce-HAP	70.12	0.00734	0.9978
3	Ce-HAP/CS	81.43	0.01071	0.9966
4	Ce-HAP/CS/BF nanocomposite	88.46	0.01354	0.9955

performance of the Ce-HAP/CS/BF composite is attributed to its efficient visible-light absorption, large surface area, well-integrated interfaces, and favourable surface morphology. These features collectively promote the generation of reactive oxygen species (ROS), which play a critical role in the photodegradation process.

The aforementioned findings make it evident the existence of surface interaction within the BF and HAP nanoparticles allows the Ce-HAP/CS/BF nanocomposite to demonstrate better photocatalytic effectiveness on MB dye decomposition. While considering the procedure affordability for a practical application perspective, the composites reliability and reusability are crucial parameters. A comparable procedure for photocatalytic reaction is used to carry down the recycling efficiency of the Ce-HAP/CS/BF nanocomposite in four sequential cycles.

To identify the primary reactive species involved in the degradation of methylene blue (MB) dye, radical trapping experiments were conducted using specific scavengers with the Ce-HAP/CS/BF nanocomposite photocatalyst. The results are displayed in Fig. 15(d). In this study, 1 mM each of $AgNO_3$, benzoquinone (BQ), and isopropanol (IPA) were used to quench electron holes (h^+), superoxide radicals ($^{\bullet}O_2^-$), and hydroxyl radicals (•OH), respectively. The degradation efficiency significantly decreased upon the addition of IPA, indicating that •OH radicals play the most critical role in the photocatalytic process under UV–visible light irradiation.

These findings highlight the strong surface interactions between the BF and HAP nanoparticles within the composite, which enhance the separation and migration of photogenerated charge carriers. As a result, the Ce-HAP/CS/BF nanocomposite exhibits improved photocatalytic performance for MB degradation.

The reusability and stability of the photocatalyst are essential for practical applications. Therefore, the recycling efficiency of the Ce-HAP/CS/BF composite was investigated over four consecutive photocatalytic cycles, as shown in Fig. 15(a). After each 100-min cycle, the photocatalyst was recovered, washed, and reused. The degradation efficiency declined slightly from 88.04 % in the first cycle to 84.4 % in the fourth cycle. This decrease may be attributed to minor losses of photocatalyst particles during recovery and the presence of ultrafine fragments that are difficult to recollect. The Ce-HAP/CS/BF ternary nanocomposite demonstrated excellent stability, with MB dye degradation efficiency decreasing only slightly from 88.46 % to 84.04 % after four cycles. The turnover number (TON × 10^3) and turnover frequency (TOF × 10^6 s^{-1}) values further confirmed its superior performance, recording 8.08, 8.01, 7.59, and 5.60 (TON) and 7.4, 7.1, 6.03, and 4.01 (TOF) for cycles one through four, respectively. These results clearly underscore the nanocomposite's high catalytic efficiency and strong potential for practical environmental pollutant remediation [66].

Structural stability of the photocatalyst was further confirmed by FTIR (Fig. 15b) and XRD analysis (Fig. 15c). The FTIR spectra before and after the fourth cycle indicate minimal changes in functional groups, suggesting chemical stability. Likewise, the XRD patterns demonstrate the preservation of crystallinity and phase composition, confirming structural robustness during repeated use.

These results suggest that the Ce-HAP/CS/BF nanocomposite is a promising, reusable, and stable material for the photocatalytic treatment of dye-contaminated wastewater. For future development, large-scale production of this nanocomposite using biogenic precursors and mesoporous architectures could offer an environmentally sustainable approach for wastewater remediation. Previous studies have similarly demonstrated the excellent photocatalytic potential of hydroxyapatite-based systems for MB dye removal, reinforcing the relevance of HAP-based materials in environmental applications.

The evaluation of the photocatalytic efficiency of the Ce-HAP/CS/BF nanocomposite was conducted and compared with several modified photocatalytic biomaterials documented in the literature (Table 3). Prior investigations have utilized diverse nanocomposites derived from biowaste materials to improve photocatalytic performance across a variety of substances [[57–65]].

The proposed photocatalytic mechanism, as depicted in Fig. 16, involves a sunlight-driven process in which the Ce-HAP/CS/BF composite acts as the active photocatalyst. Upon irradiation with sunlight, photons are absorbed, promoting electrons from the valence band (VB) to the conduction band (CB) of the catalyst, creating electron-hole pairs. The excited electrons in the CB have the potential to reduce molecular oxygen (O_2) to form reactive oxygen species (ROS) such as superoxide radicals ($O_2^{\bullet-}$). Meanwhile, the holes in the VB interact with water molecules or hydroxide ions (OH^-) to produce hydroxyl radicals ($^{\bullet}OH$) through an oxidation process. These highly reactive species, including $O_2^{\bullet-}$ and $^{\bullet}OH$, engage in the degradation of organic pollutants adsorbed on the catalyst's surface, converting them into less harmful substances like carbon dioxide (CO_2) and water (H_2O). This overall mechanism emphasizes the synergistic effect of the Ce-HAP/CS/BF nanocomposite in promoting efficient separation and transfer of photo-generated charges, enhancing photocatalytic activity under visible light irradiation for effective pollutant degradation.

Under visible light, the Ce-HAP/CS/BF photocatalyst initiates a series of redox reactions leading to the degradation of organic pollutants such as methylene blue (MB) dye and doxycycline.

Photoexcitation of the catalyst:

$$\text{Ce} - \text{HAP/CS/BF} + h\nu \longrightarrow e^- + h^+ \quad (6)$$

Reduction of oxygen to superoxide radicals:

$$e^- + O_2 \longrightarrow \bullet O_2 \quad (7)$$

Oxidation of water molecules to hydroxyl radicals:

$$h^+ + H_2O \longrightarrow OH \bullet + H^+ \quad (8)$$

Oxidative degradation of MB dye by hydroxyl radicals:

Table 3
Comparison of photocatalytic efficiency of Ce-HAP/CS/BF nanocomposite with various photocatalysts for MB dye.

S. no	Samples	Organic dyes	Time (mins)	Efficiency (%)	Reference
1	CeO_2/V_2O_5	MB 300	MB 300	~ 76.8	[57]
2	Graphite/TiO_2	MB 240	MB 240	~ 85	[58]
3	g-C_3N_4 /TiO_2 composite	MB 156	MB 156	~ 90	[59]
4	g-C_3N_4 thin layer @ CeO_2 nanocomposite	Doxycycline drug 60	Doxycycline drug 60	~ 84	[60]
5	titanium-doped hydroxyapatite	MB 240	MB 240	~ 93	[61]
6	Ag_3PO_4/ HAp@γ-Fe_2O_3 nanocomposite	MB 240	MB 240	~ 99	[62]
7	ZnO nanoparticles	Doxycycline drug 300	Doxycycline drug 300	~ 99	[63]
8	$Cu_2O/BiVO_4$ composite	MB 160	MB 160	~ 72.9	[64]
9	HAp/g-C_3N_4 composite	MB 100	MB 100	93.69	[65]
10	Ce-HAP/CS/BF nanocomposite	MB 100	MB 100	88.46	This work

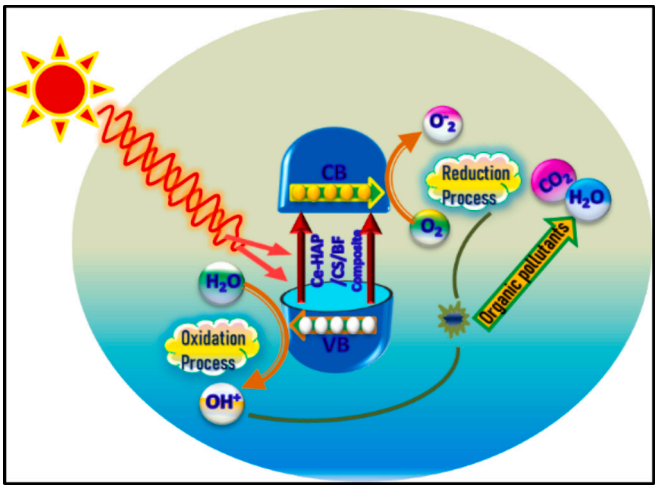

Fig. 16. Possible photocatalytic degradation mechanism of Ce-HAP/CS/BF composite against MB organic dye.

$$OH\bullet + \text{MB dye} \longrightarrow \text{Degradation products} \quad (9)$$

Oxidative degradation of doxycycline by hydroxyl radicals:

$$OH\bullet + \text{Doxycycline} \longrightarrow \text{Degradation products} \quad (10)$$

Degradation of doxycycline by superoxide radicals:

$$O_2^- + \text{Doxycycline} \longrightarrow CO_2 + H_2O + \text{other byproducts} \quad (11)$$

Degradation of MB dye by superoxide radicals:

$$O_2^- + \text{MB dye} \longrightarrow CO_2 + H_2O + \text{other byproducts} \quad (12)$$

4. Conclusion

This study successfully demonstrated the synthesis of hydroxyapatite using snail shells and BF via a simple precipitation method to develop a novel Ce-HAP/CS/BF nanocomposite. The resulting material exhibited a regular spherical-shaped mesoporous morphology, enhanced mechanical strength, and notable antibacterial activity, with particle sizes ranging from 200 to 260 nm. Structural and functional characterizations-including XRD, FTIR, FE-SEM, TEM, and antibacterial assays-confirmed the effective integration of all composite constituents. The Ce-HAP/CS/BF nanocomposite exhibited excellent photocatalytic performance by degrading methylene blue dye under UV irradiation, achieving 88.4 % degradation efficiency within 100 min. Furthermore, the composite demonstrated substantial stability and reusability, showing minimal efficiency loss after successive treatment cycles. Collectively, the results underscore the Ce-HAP/CS/BF nanocomposites potential as a sustainable, cost-effective, and eco-friendly material for wastewater treatment. Developed entirely from biogenic and renewable resources, this multifunctional composite offers an innovative approach for the efficient removal of toxic dyes from industrial effluents. Its superior photocatalytic and antibacterial properties also suggest broader applicability in environmental remediation technologies, contributing to greener and more resilient water purification strategies.

CRediT authorship contribution statement

Raji Ramachandran: Writing – original draft, Software, Resources, Methodology, Formal analysis, Conceptualization. **P. Saravanakumar:** Writing – review & editing, Software, Methodology, Formal analysis, Data curation. **M. Mathina:** Writing – review & editing, Visualization, Software, Methodology, Data curation. **E. Shinyjoy:** Writing – review & editing, Visualization, Software, Resources, Investigation, Data curation. **Zarlina Zainuddin:** Writing – review & editing, Visualization, Validation, Supervision, Software, Formal analysis. **R.K. Govindarajan:** Writing – review & editing, Visualization, Resources, Methodology, Data curation. **Chinnaperumal Kamaraj:** Writing – review & editing, Visualization, Validation, Supervision, Software, Resources, Methodology, Conceptualization. **Dhanaraj Gopi:** Writing – review & editing, Visualization, Supervision, Software, Resources, Data curation. **Ratna Surya Alwi:** Writing – review & editing, Visualization, Supervision, Project administration, Funding acquisition, Formal analysis.

Declaration of competing interest

The authors declare that they have no known competing financial interests or personal relationships that could have appeared to influence the work reported in this paper.

Acknowledgments

The authors acknowledge the postdoctoral program of the National Research and Innovation Agency (BRIN) (Grant No. 114/II/HK/2024), awarded to Dr. Raji Ramachandran. They also express their gratitude for the scientific and technical support provided by the Research Centre for Computing, BRIN, through the E-Layanan Sains BRIN, Indonesia.

Data availability

Data will be made available on request.

References

[1] N.R.J. Hynes, J.S. Kumar, H. Kamyab, J.A.J. Sujana, O.A. Al-Khashman, Y. Kuslu, A. Ene, B. Suresh Kumar, Modern enabling techniques and adsorbents based dye removal with sustainability concerns in textile industrial sector - a comprehensive review, J. Clean. Prod. 272 (2020) 122636, https://doi.org/10.1016/j.jclepro.2020.122636.
[2] F. Hu, H. Yang, L. Qiu, X. Wang, Z. Ren, S. Wei, H. Zhou, Y. Chen, H. Hu, Innovation networks in the advanced medical equipment industry: supporting regional digital health systems from a local–national perspective, Front. Public Health 13 (2025) 1635475, https://doi.org/10.3389/fpubh.2025.1635475.
[3] S.P. Padinhattath, J. Govindaraj, R.L. Gardas, Exploring non-stoichiometric pseudoprotic ionic liquid for effective elimination of cationic dyes from textile effluent: a circular approach, J Water Process Eng 58 (2024) 104921, https://doi.org/10.1016/j.jwpe.2024.104921.
[4] H. Badamasi, S.O. Sanni, O.T. Ore, A.A. Bayode, D.T. Koko, O.K. Akeremale, S. S. Emmanuel, Eggshell waste materials-supported metal oxide nanocomposites for the efficient photocatalytic degradation of organic dyes in water and wastewater: a review, Bioresour. Technol. Rep. 26 (2024) 101865, https://doi.org/10.1016/j.biteb.2024.101865.
[5] H. Ben Slama, A. Chenari Bouket, Z. Pourhassan, F.N. Alenezi, A. Silini, H. Cherif-Silini, T. Oszako, L. Luptakova, P. Golińska, L. Belbahri, Diversity of synthetic dyes from textile industries, discharge impacts and treatment methods, Appl. Sci. 11 (2021) 6255, https://doi.org/10.3390/app11146255.
[6] M.F. Lanjwani, M. Tuzen, M.Y. Khuhawar, T.A. Saleh, Trends in photocatalytic degradation of organic dye pollutants using nanoparticles: a review, Inorg. Chem. Commun. 159 (2024) 111613, https://doi.org/10.1016/j.inoche.2023.111613.
[7] S. Dutta, S. Adhikary, S. Bhattacharya, D. Roy, S. Chatterjee, A. Chakraborty, D. Banerjee, A. Ganguly, S. Nanda, P. Rajak, Contamination of textile dyes in aquatic environment: adverse impacts on aquatic ecosystem and human health, and its management using bioremediation, J. Environ. Manag. 353 (2024) 120103, https://doi.org/10.1016/j.jenvman.2024.120103.
[8] S. Parida, A.K. Mandal, A.K. Behera, S. Patra, R. Nayak, C. Behera, M. Jena, A comprehensive review on phycoremediation of azo dye to combat industrial wastewater pollution, J Water Process Eng 70 (2025) 107088, https://doi.org/10.1016/j.jwpe.2025.107088.
[9] A.P. Periyasamy, Recent advances in the remediation of textile-dye-containing wastewater: prioritizing human health and sustainable wastewater treatment, Sustainability 16 (2024) 495, https://doi.org/10.3390/su16020495.
[10] Z. Jiang, X. Han, C. Zhao, S. Wang, X. Tang, Recent advance in biological responsive nanomaterials for biosensing and molecular imaging application, Int. J. Mol. Sci. 23 (3) (2022) 1923, https://doi.org/10.3390/ijms23031923.
[11] P.O. Oladoye, T.O. Ajiboye, E.O. Omotola, O.J. Oyewola, Methylene blue dye: toxicity and potential elimination technology from wastewater, Results Eng. 16 (2022) 100678, https://doi.org/10.1016/j.rineng.2022.100678.
[12] M.M. Islam, A.R. Aidid, J.N. Mohshin, H. Mondal, S. Ganguli, A.K. Chakraborty, A critical review on textile dye-containing wastewater: ecotoxicity, health risks, and remediation strategies for environmental safety, Clean. Chem. Eng. 11 (2025) 100165, https://doi.org/10.1016/j.clce.2025.100165.

[13] R. Ramachandran, M. Alsawalha, T. Alomayri, P. Thangavelu, S. Maytasya, A. D. Yunianti, R.S. Alwi, Sustainable fabrication of Ti alloy-coated NiO/Ag bimetallic nanoparticles incorporated with Calotropis gigantea fiber: a dual-purpose material for efficient environmental pollutant degradation and advanced biomedical applications, Surf Interfaces 60 (2025) 105995, https://doi.org/10.1016/j.surfin.2025.105995.
[14] R. Ramachandran, S. Ramya, E. Shinyjoy, L. Kavitha, D. Gopi, Biocomposite coating of Wrightia tinctoria root bark fiber reinforced samarium substituted hydroxyapatite/ polypyrrole on titanium for potential orthopedic applications, Mater. Chem. Phys. 289 (2022) 126447, https://doi.org/10.1016/j.matchemphys.2022.126447.
[15] S.T. Nipa, N.R. Shefa, S. Parvin, M.A. Khatun, M.J. Alam, S. Chowdhury, M.A. R. Khan, S.M.A.Z. Shawon, B.K. Biswas, M.W. Rahman, Adsorption of methylene blue on papaya bark fiber: equilibrium, isotherm and kinetic perspectives, Results Eng. 17 (2023) 100857, https://doi.org/10.1016/j.rineng.2022.100857.
[16] V. Arumugaperumal, S. K, Solar light driven photocatalytic degradation of methylene blue dye over Cu doped α-MnO_2 nanoparticles, Chemical Physics Impact 8 (2024) 100434, https://doi.org/10.1016/j.chphi.2023.100434.
[17] S. Li, Y. Cui, M. Wen, G. Ji, Toxic effects of methylene blue on the growth, reproduction and physiology of *Daphnia magna*, Toxics 11 (2023) 594, https://doi.org/10.3390/toxics11070594.
[18] A.R. Khan, H. Tahir, F. Uddin, U. Hameed, Adsorption of methylene blue from aqueous solution on the surface of wool fiber and cotton fiber, J. Appl. Sci. Environ. Manag. 9 (2005), https://doi.org/10.4314/jasem.v9i2.17287.
[19] M.A. Al-Nuaim, A.A. Alwasiti, Z.Y. Shnain, The photocatalytic process in the treatment of polluted water, Chem. Pap. 77 (2023) 677–701, https://doi.org/10.1007/s11696-022-02468-7.
[20] Y. González, G. Gómez, G.E. Moeller-Chávez, G. Vidal, UV disinfection systems for wastewater treatment: emphasis on reactivation of microorganisms, Sustainability 15 (2023) 11262, https://doi.org/10.3390/su151411262.
[21] A. Ahmad, A. e Noor, A. Anwar, S. Majeed, S. Khan, Z. Ul Nisa, S. Ali, L. Gnanasekaran, S. Rajendran, H. Li, Support based metal incorporated layered nanomaterials for photocatalytic degradation of organic pollutants, Environ. Res. (2024) 119481, https://doi.org/10.1016/j.envres.2024.119481.
[22] R.N.A. Andriambahiny, J. Das, B. Roy, B. Lodh, B. Pal, A review on the recent advancement of acid modified bio-adsorbents for the removal of methyl orange dye from wastewater treatment, Discov. Chem. 2 (2025) 92, https://doi.org/10.1007/s44371-025-00180-5.
[23] S.A. Mohammadi, H. Najafi, S. Zolgharnian, S. Sharifian, N. Asasian-Kolur, Biological oxidation methods for the removal of organic and inorganic contaminants from wastewater: a comprehensive review, Sci. Total Environ. 843 (2022) 157026, https://doi.org/10.1016/j.scitotenv.2022.157026.
[24] O. Makota, E. Dutková, J. Briančin, J. Bednarcik, M. Lisnichuk, I. Yevchuk, I. Melnyk, Advanced photodegradation of azo dye methyl orange using H_2O_2-activated Fe_3O_4@SiO_2@ZnO composite under UV treatment, Molecules 29 (2024) 1190, https://doi.org/10.3390/molecules29061190.
[25] S. Kainth, P. Sharma, O.P. Pandey, Green sorbents from agricultural wastes: a review of sustainable adsorption materials, Appl Surf Sci Adv 19 (2024) 100562, https://doi.org/10.1016/j.apsadv.2023.100562.
[26] B. Gonçalves, M. Camillo, M. Oliveira, L. Carreira, J. Moulin, H. Fantuzzi Neto, B. de Oliveira, A. Pereira, S. Monteiro, Surface treatments of coffee husk fiber waste for effective incorporation into polymer biocomposites, Polymers (Basel) 13 (2021) 3428, https://doi.org/10.3390/polym13193428.
[27] K. Chaturvedi, M. Dhangar, M. Mili, A.K. Srivastava, S. Verma, Synthesis and studies of advanced adsorbent zeolites by using red mud and rice husk ash as a thermal insulation agent, Arab. J. Geosci. 18 (2025) 105, https://doi.org/10.1007/s12517-025-12241-1.
[28] P. Xia, Y.-J. Song, Y.-Z. Liu, M.-X. Long, C. Yang, X.-Y. Zhang, T. Zhang, Advances in the optical and electronic properties and applications of bismuth-based semiconductor materials, J. Mater. Chem. C 12 (2024) 1609–1624, https://doi.org/10.1039/D3TC03329E.
[29] Muhammad Asnawir Nasution, Iwantono, Puji Nurrahmawati, Nashiha Chalvi Syahra, Sulistyo Rini, Suratun Nafisah, Romi Fadli Syahputra, Marlia Morsin, The enhancement light absorption of ZnO-TiO2 nanocomposite as photoanode, Int. J. Nanoelectron. Mater. 16 (2024) 883–890, https://doi.org/10.58915/ijneam.v16i3.1374.
[30] R.L.P. Rocha, L.M.C. Honorio, R.D. de S. Bezerra, P. Trigueiro, T.M. Duarte, M. G. Fonseca, E.C. Silva-Filho, J.A. Osajima, Light-activated hydroxyapatite photocatalysts: new environmentally-friendly materials to mitigate pollutants, Minerals 12 (2022) 525, https://doi.org/10.3390/min12050525.
[31] H. Li, Y. Jiang, Y. Wang, H. Lv, H. Xie, G. Yang, T. Tang, The effects of warfarin on the pharmacokinetics of senkyunolide I in a rat model of biliary drainage after administration of Chuanxiong, Front. Pharmacol. 9 (2018) 1461, https://doi.org/10.3389/fphar.2018.01461.
[32] A. Abdelmoaty, S. Mousa, Synthesis and characterization of hydroxyapatite nanoparticles from calcium hydroxide fouled with gases evolved from smokestack of glass industry, Sci. Rep. 14 (2024) 10969, https://doi.org/10.1038/s41598-024-60970-2.
[33] S. Latifi, S. Saoiabi, M.M. Alanazi, O. Boukra, A. Krime, L. El Hammari, K. Azzaoui, B. Hammouti, G. Hanbali, S. Jodeh, A. Saoiabi, R. Sabbahi, M. Algarra, N. Abidi, Low-cost titania-hydroxyapatite (TiHAp) nanocomposites were synthesized for removal of methylene blue under solar and UV irradiation, Next Mater. 8 (2025) 100859, https://doi.org/10.1016/j.nxmate.2025.100859.
[34] P. Saravanakumar, R. Ramachandran, R.S. Alwi, D. Gopi, Eco-friendly synthesis of dual-layer coated cerium oxide nanoparticles and holmium-substituted hydroxyapatite/polyacrylic acid composite on titanium implants for biomedical applications, Inorg. Chem. Commun. 178 (2025) 114480, https://doi.org/10.1016/j.inoche.2025.114480.
[35] R. Raji, S. Elangomannan, R. Subramani, K. Louis, M. Periasamy, G. Dhanaraj, Calotropis Gigantea fiber—a biogenic reinforcement material for Europium substituted hydroxyapatite/poly(3,4-propylenedioxythiophene) matrix: a novel ternary composite for biomedical applications, ACS Omega 7 (2022) 6024–6034, https://doi.org/10.1021/acsomega.1c06372.
[36] F. Wu, D.D.W. Lin, J.H. Chang, C. Fischbach, L.A. Estroff, D. Gourdon, Effect of the materials properties of hydroxyapatite nanoparticles on fibronectin deposition and conformation, Cryst. Growth Des. 15 (2015) 2452–2460, https://doi.org/10.1021/acs.cgd.5b00231.
[37] M. Senthilkumar, S.K. Ramachandran, K.L. Servarayan, A. Periyasamy, V. V. Sivasamy, E. Sundaram, Isolation of chitosan and hydroxyapatite from waste edible white garden snail shells and their sensing applications towards industrial Congo red dye detection: greener approach, Int. J. Biol. Macromol. 275 (2024) 133483, https://doi.org/10.1016/j.ijbiomac.2024.133483.
[38] R. Ramachandran, E. Shinyjoy, S. Ramya, L. Kavitha, D. Gopi, Leucas aspera assisted green synthesis of mineralized hydroxyapatite/polycaprolactone: a potential composite for biomedical applications, Mater. Lett. 326 (2022) 132972, https://doi.org/10.1016/j.matlet.2022.132972.
[39] R.S. Alwi, R. Gopinathan, A. Bhowal, C. Garlapati, Adsorption characteristics of activated carbon for the reclamation of eosin Y and Indigo carmine colored effluents and new isotherm model, Molecules 25 (2020) 6014, https://doi.org/10.3390/molecules25246014.
[40] H. Li, Y. Zhou, L. Liao, H. Tan, Y. Li, Z. Li, B. He, Pharmacokinetics effects of Chuanxiong rhizoma on Warfarin in pseudo germ-free rats, Front. Pharmacol. 13 (2023) 1022567, https://doi.org/10.3389/fphar.2022.1022567.
[41] W. Zhou, Y. Sheng, A. Alizadeh, S. Baghaei, Q. Lv, M. Shamsborhan, N. Nasajpour-Esfahani, R. Rezaie, Synthesis and characterization of Alg/Gel/n-HAP/MNPs porous nanocomposite adsorbent for efficient water conservancy and removal of methylene blue in aqueous environments: kinetic modeling and artificial neural network predictions, J. Environ. Manag. 349 (2024) 119446, https://doi.org/10.1016/j.jenvman.2023.119446.
[42] S. Sridevi, S. Sutha, L. Kavitha, D. Gopi, Physicochemical and biological behaviour of biogenic derived hydroxyapatite and carboxymethyl cellulose/sodium alginate biocomposite coating on Ti6Al4V alloy for biomedical applications, Mater. Chem. Phys. 254 (2020) 123455, https://doi.org/10.1016/j.matchemphys.2020.123455.
[43] J. Cheng, C. Bi, X. Zhou, D. Wu, D. Wang, C. Liu, Z. Cao, Preparation of bamboo-based activated carbon via steam activation for efficient methylene blue dye adsorption: modeling and mechanism studies, Langmuir 39 (2023) 14119–14129, https://doi.org/10.1021/acs.langmuir.3c01972.
[44] J. Ajayan, P. Mohankumar, D. Nirmal, L.M.I.L. Joseph, S. Bhattacharya, S. Sreejith, S. Kollem, S. Rebelli, S. Tayal, B. Mounika, Ferroelectric field effect transistors (FeFETs): advancements, challenges and exciting prospects for next generation Non-Volatile Memory (NVM) applications, Mater Today Commun 35 (2023) 105591, https://doi.org/10.1016/j.mtcomm.2023.105591.
[45] M. Jawaid, S.S. Chee, M. Asim, N. Saba, S. Kalia, Sustainable kenaf/bamboo fibers/clay hybrid nanocomposites: properties, environmental aspects and applications, J. Clean. Prod. 330 (2022) 129938, https://doi.org/10.1016/j.jclepro.2021.129938.
[46] S. Cheng, H. Zhang, X. Chen, Y. Wang, F. Cheng, P. Sun, B. Lu, Electric-assisted coaxial wet spinning of radially oriented Boron nitride nanosheet-based composite fiber with highly enhanced piezoelectricity, Adv. Fiber Mater. 7 (4) (2025) 1302–1316, https://doi.org/10.1007/s42765-025-00567-0.
[47] H. Chen, J. Xu, Y. Li, T. Zhang, F. Qiu, X. Huang, Trash to treasure: from construction waste to tellurium adsorbent materials, J. Clean. Prod. 312 (2021) 127752, https://doi.org/10.1016/j.jclepro.2021.127752.
[48] A.M. Ahmed, M.L. Mekonnen, K.N. Mekonnen, Review on nanocomposite materials from cellulose, chitosan, alginate, and lignin for removal and recovery of nutrients from wastewater, Carbohydr. Polym. Technol. Appl. 6 (2023) 100386, https://doi.org/10.1016/j.carpta.2023.100386.
[49] N.P. Simelane, J.K.O. Asante, P.P. Ndibewu, A.S. Mramba, L.L. Sibali, Biopolymer composites for removal of toxic organic compounds in pharmaceutical effluents – a review, Carbohydr. Polym. Technol. Appl. 4 (2022) 100239, https://doi.org/10.1016/j.carpta.2022.100239.
[50] M.A. Kaczorowska, D. Bożejewicz, The application of chitosan-based adsorbents for the removal of hazardous pollutants from aqueous solutions—a review, Sustainability 16 (2024) 2615, https://doi.org/10.3390/su16072615.
[51] Z. Huang, Y. Qu, X. Hua, F. Wang, X. Jia, L. Yin, Recent advances in soybean protein processing technologies: a review of preparation, alterations in the conformational and functional properties, Int. J. Biol. Macromol. 248 (2023) 125862, https://doi.org/10.1016/j.ijbiomac.2023.125862.
[52] H. Liang, C. Lv, H. Chen, L. Wu, X. Hou, Facile synthesis of chitosan membranes for visible-light-driven photocatalytic degradation of tetracycline hydrochloride, RSC Adv. 10 (2020) 45171–45179, https://doi.org/10.1039/D0RA08358E.
[53] V. Selvam, T. Jeyapaul, K. Prakash, K. Shanthini, C. Anitha, Metal-free and fully recoverable MWCNT/g-C3N4 /chitosan nanocomposite thin film with excellent photocatalytic activity against organic pollutant degradation, Phys. B Condens. Matter 655 (2023) 414726, https://doi.org/10.1016/j.physb.2023.414726.
[54] K.P. Valli, A.A.C. Raja, V. Selvam, S.M.J. Kala, A.S. Joy Sinthiya, B. Malathi, Evaluating the photocatalytic efficiency of polypyrrole-enhanced Bi_2WO_6/g-C_3N_5 nanocomposites for effective organic pollutant degradation, Next Mater. 8 (2025) 100557, https://doi.org/10.1016/j.nxmate.2025.100557.
[55] M. Dadmehr, B. Korouzhdehi, A. Tavassoli, M. Malekkiani, Photocatalytic activity of green synthesized cadmium sulfide quantum dots on the removal of RhB dye and

its cytotoxicity and antibacterial studies, Nanotechnology 33 (2022) 395101, https://doi.org/10.1088/1361-6528/ac79bc.
[56] M. Malekkiani, A.H.J. Magham, F. Ravari, M. Dadmehr, Enhanced ultraviolet driven photocatalytic activity of CTS-SnO2-MWCNTs ternary nanohybrid for photodegradation of methylene blue and bacteria in aqueous solutions, Environ. Technol. Innov. 34 (2024) 103559, https://doi.org/10.1016/j.eti.2024.103559.
[57] D.-T. Tran, T.-H. Ha, T.-P.-T. Vu, V.-N. Nguyen, T.-D. Pham, Novel CeO2-V2O5/rGO tertiary photocatalyst for improved cefotaxime degradation using visible-light, Inorg. Chem. Commun. 161 (2024) 112044, https://doi.org/10.1016/j.inoche.2024.112044.
[58] B.B. Shaik, N.K. Katari, J.K. Raghupathi, S.B. Jonnalagadda, S. Rana, Titanium dioxide/graphene-based nanocomposites as photocatalyst for environmental applications: a review, ChemistrySelect 9 (2024), https://doi.org/10.1002/slct.202403521.
[59] K. Aziz, A. Naz, S. Manzoor, M.I. Khan, A. Shanableh, J. Fernandez Garcia, Visible light photodegradation of glyphosate and methylene blue using defect-modified graphitic carbon nitride decorated with Ag/TiO2, Catalysts 13 (2023) 1087, https://doi.org/10.3390/catal13071087.
[60] W. Liu, J. Zhou, Z. Hu, Nano-sized g-C_3N_4 thin layer@CeO_2 sphere core-shell photocatalyst combined with H_2O_2 to degrade doxycycline in water under visible light irradiation, Sep. Purif. Technol. 227 (2019) 115665, https://doi.org/10.1016/j.seppur.2019.06.003.
[61] N. Mendez, M. Apátiga-Castro, E. Pérez-Ramírez, M. de la Luz-Asunción, K. Soto, A. Manzano-Ramírez, A. de J. Ruiz - Baltazar, Efficient Degradation of Methylene Blue Using Titanium-Substituted Hydroxyapatite for Water Purification, 2025, https://doi.org/10.2139/ssrn.5090589.
[62] A.J. Somasundaram, E. Elanthamilan, S.-F. Wang, I. Sharmila Lydia, Construction of magnetic Ag3PO4/Fe3O4/chitosan polymer composite with enhanced visible-light-driven photocatalytic activity for the methylene blue dye degradation, J. Polym. Environ. 32 (2024) 6650–6666, https://doi.org/10.1007/s10924-024-03375-6.
[63] I.J. Ani, U.G. Akpan, M.A. Olutoye, B.H. Hameed, T.C. Egbosiuba, Adsorption–photocatalysis synergy of reusable mesoporous TiO2–ZnO for photocatalytic degradation of doxycycline antibiotic, Heliyon 10 (2024) e30531, https://doi.org/10.1016/j.heliyon.2024.e30531.
[64] M. Liaqat, T. Iqbal, Z. Ashfaq, S. Afsheen, R.R. Mahmood Khan, M.A. Sayed, A. M. Ali, Comparative photocatalytic study of visible light driven BiVO4, Cu2O, and Cu2O/BiVO4 nanocomposite for degradation of antibiotic for wastewater treatment, J. Chem. Phys. 159 (2023), https://doi.org/10.1063/5.0176106.
[65] P. Govindasamy, B. Kandasamy, P. Thangavelu, S. Barathi, M. Thandavarayan, M. Shkir, J. Lee, Biowaste derived hydroxyapatite embedded on two-dimensional g-C3N4 nanosheets for degradation of hazardous dye and pharmacological drug via Z-scheme charge transfer, Sci. Rep. 12 (2022) 11572, https://doi.org/10.1038/s41598-022-15799-y.
[66] M. Malekkiani, A. Heshmati Jannat Magham, F. Ravari, M. Dadmehr, Facile fabrication of ternary MWCNTs/ZnO/Chitosan nanocomposite for enhanced photocatalytic degradation of methylene blue and antibacterial activity, Sci. Rep. 12 (2022) 5927, https://doi.org/10.1038/s41598-022-09571-5.